ORIGINAL PAPER

An Inverted Heterogeneous Velocity Model for Microseismic Source Location in Deep Buried Tunnels

Liu Liu[1] · Shaojun Li[1] · Yaxun Xiao[1] · Shujie Chen[1] · Zhaofeng Wang[1] · Guangliang Feng[1] · Yao Wang[2]

Abstract

Microseismic (MS) monitoring is an effective and widely applied technology for early warning and prevention of rockburst disasters in deeply buried tunnels. The location of the microseismic source is the top priority of MS monitoring. However, an unknown complex and consistently changing velocity distribution of surrounding rocks is a major challenge for accurate MS source location. A real-time velocity inversion method of monitoring areas during tunnel drilling is urgently needed to provide a newly updated heterogenous velocity model. This paper develops a velocity inversion strategy for surrounding rocks using drilling and blasting seismic data. Inverted heterogeneous velocity models can be obtained at multiple construction stages with drilling. An L2 norm double-difference location method based on the simplex optimization method is provided for MS location using heterogeneous velocity models. Numerical studies test the accuracy of the proposed velocity inversion and MS location method. Noticeable improvement in location accuracy can be observed using updating inverted heterogeneous velocity models. Finally, we conducted a field experiment at two new tunnels with a burial depth of 2400 m in the China Jinping Underground Laboratory Phase II. Multiple blasting sources with known coordinates verified the performance of the proposed MS location method.

1 Introduction

A growing number of deep buried tunnels have been constructed worldwide for transportation, hydropower, and mining. However, rockburst, one of the most dangerous disasters in deep projects, occurs more frequently as the buried depth of the tunnel increases (Dai et al. 2017). For example, an extremely intense rockburst on November 28, 2009 in a 2525 m deep buried drainage tunnel of the Jinping II hydropower station in China featured several sudden and violent collapses of rock mass under high-stress conditions, causing severe casualties, destroying the tunnel boring machine, and delaying the construction schedule (Li et al. 2012; Feng et al.

2019). Previous studies have revealed a strong relationship between the evolution of microseismicity and the occurrence of high-strength rockburst (Li et al. 2017; Dai et al. 2018). Thus, microseismic (MS) monitoring techniques have been widely introduced in deep tunnel engineering to trace rock fractures and provide early warning of rockburst disasters (Xiao et al. 2016; Ma et al. 2019).

MS source location is the priority of MS monitoring and subsequent rockburst warning (Li et al. 2011; Ma et al. 2022). The accurate MS source location and the evaluation of MS parameters during construction provide essential information to reveal the distribution of the surrounding rock fracture network and the potential failure pattern of the rock mass (Pei et al. 2009; Hu and Dong 2019; Pu et al. 2022). The source location method of multiple scales from earthquakes and MS to acoustic emission (AS) sources has been studied for over a century (Geiger 1912). With the rapid improvement in calculation methods and hardware, researchers have explored many classic location methods, including the Geiger method (Geiger 1912), the US Bureau of Mines (USBM) method (Leighton and Blake 1970), Thueber's

✉ Shaojun Li
  sjli@whrsm.ac.cn

1 State Key Laboratory of Geomechanics and Geotechnical Engineering, Institute of Rock and Soil Mechanics, Chinese Academy of Sciences, Wuhan 430071, China

2 Department of Civil and Coastal Engineering, University of Florida, Gainesville, FL 32611, USA

method (Thueber 1985), the simplex method (Prugger and Gendzwill 1988), and the double residue difference method (Waldhauser and Ellsworth 2000). Note that the location accuracy relies strongly on a velocity model of the monitoring area. A single-velocity model can be applied in a simple and homogeneous lithology project but yields significant location errors in more complex geological settings. Feng et al. (2015a) proposed a sectional velocity model method for MS location and reported several successful application cases in tunnel projects. Castellanos and Van der Baan (2015) proposed a cross-correlation location method in mines. Collins et al. (2014) established a velocity model considering different infills of voids. Jiang et al. (2021) introduced a fast-marching method with a second-order difference approach (FMM2) as a forward modeling method employing the traveling time, making MS location possible using a velocity model containing a cavern. Dong et al. (2019, 2020) provided a velocity-free MS location method to mitigate the influence of wave velocity. The method locates the MS source in the mine without premeasured velocity, which is a beneficial complement to the traditional locating theory. However, there are still some challenges of MS source location in a deep tunnel, especially when the sensor network is placed near the drilling face. (1) Complex velocity models, such as the excavation damaged zone (EDZ) (Li et al. 2013), substantially change the ray path of the seismic wave traveling along the sidewall of the deep tunnel. To accurately calculate the travel time, a velocity model representing the characteristics of the EDZ is needed during the location. (2) The acquisition geometry of the MS monitoring network is ill-posed. Velocity analysis and inversion methods in mining and earthquake engineering are not applicable to linear observation acquisition in tunnels. (3) The condition of the surrounding rock changes dramatically over time during excavation. Continually updating velocity must be inverted while tunnelling to provide better location resolution.

The blasting source of tunnel excavation provides meaningful waveform information that can enable active seismic exploration without an accurate trigger time. Experiments and numerical studies (Leparoux et al. 2012) suggest that the EDZ underneath a concrete layer can be investigated with surface waves traveling along tunnel sidewalls. The S-wave velocity model can be estimated by inversion of the fundamental mode of the Rayleigh wave (Czarny et al. 2021). Then, the trigger time of blasting can be estimated by the inverted S-wave velocity. In that case, multiple blasting sources can be used for P-wave first-arrival traveltime tomography, which can continually invert the heterogeneous P-wave velocity during the whole tunnelling construction. Previous works (Dong et al. 2022) suggest a significant application of abnormal region identification in rock-mass using traveltime tomography, which provided insight into potential hazards detection in underground geotechnical engineering. However, first-arrival traveltime tomography is still challenging using an ill-posed acquisition system and limited blasting source. First-arrival traveltime tomography can be classified as traditional ray tracing-based tomography and the adjoint-state method (Sei and Symes 1994) depending on whether the ray path calculations are explicit or implicit. Ray tracing-based methods employ the straight-line method, curve method, or shortest path ray tracing method as a forward modeling operator. The least-square conjugate-gradient method (LSQR) (Yao et al. 1999) and simultaneous iterative reconstruction (SIRT) (Gregor and Benson 2008) are applied in the inversion of ray-tracing-based tomography. The velocity model updates are obtained by solving the tomographic equations. The definition and theory of traditional ray tracing-based inversion are clear, but the solution of tomographic equations is highly ill-conditioned and unstable. The adjoint-state method of first-arrival traveltime tomography, incorporated in the implicit ray tracing calculation, is provided by Taillandier et al. (2009) for surface seismic surveys. The gradient is calculated by dual modeling based on solving the eikonal equation using the fast-marching method (FMM) (Kroon 2021) or fast sweeping method (FSM) (Zhao 2005). Compared to the ray tracing method, the adjoint-state method has the advantage of imaging complex geological environments with limited pairs of sources and receivers.

In this work, we fully use drilling and blasting source data and developed an MS source location method in deep buried tunnels using an updated inverted heterogeneous velocity model. An improved perturbational dispersion inversion method is developed by combining a modified thin layer method (TLM) forward simulation and perturbational inversion method, which can estimate the S-wave velocity model and the depth of the EDZ. The starting time t_0 of blasting sources is calculated using S-wave back propagation tracing by the FMM on the inverted S-wave model. An adjoint-state first arrival tomography method is provided to continually invert the heterogeneous P-wave velocity model. A double-difference simplex-based method is introduced for MS location source. A realistic numerical study based on the finite difference in the time domain (FDTD) is used to visualize the blasting source wavefield in the surrounding rock. Sixty-four MS sources around the tunnel drilling face are used to test the accuracy of the proposed location method. A field experiment is conducted at two new tunnels with a buried depth of 2400 m in China Jinping Underground Laboratory Phase II. Blasting sources with known locations are used to test the performance of the proposed location method in practice.

2 Methodology

2.1 Motivation

Obtaining a reliable velocity model of the monitoring area is the priority of MS source location. The velocity model determines the wave propagation path and arrival time, which significantly impacts the accuracy of the location. The presence of an EDZ, the discontinuity of the rock mass and different intactness and stress conditions make the wave propagation path complex. Figure 1 presents the influence of the EDZ on wave propagation as an example. The wave propagation is represented by straight lines connecting sources and sensors if the velocity model is homogeneous (Fig. 1a). However, a zone that features lower velocity can be observed near the existing tunnel when the EDZ is considered, as shown in Fig. 1b. The propagation paths in the heterogenous velocity model are calculated by the FMM, and the paths follow Fermat's principle of least time. The wave transmitted at the source travels toward the high-velocity area and backward to the sensors. The propagation paths in Fig. 1b are longer than the straight lines shown in Fig. 1a. The assumption of the homogeneous velocity model can cause location errors of MS events.

In the case shown in Fig. 1, a new tunnel is planned at an existing tunnel constructed for several years. The development of the EDZ and its effect on actual wave propagation paths cannot be ignored during MS location. However, it is possible to invert the velocity model by the drilling blast source of the new proposal tunnel. A drilling and blasting source can be used for active seismic exploration with an unknown accurate starting time of the source. Dispersion analysis of surface waves traveling along the tunnel sidewall and first-arrival traveltime tomography are two potential technologies in seismic exploration that can invert the S-wave and P-wave velocities. Extraction of the dispersion curve using limited sensors and determination of the starting timepoint t_0 during tomography are two critical steps during the inversion of velocity. We develop an inversion velocity model method and a double-difference MS location method in this study. The proposed method aims to visualize the heterogenous velocity field using ongoing drilling and blasting signals and enhance the accuracy of MS location using the updated inverted heterogenous velocity.

2.2 Overall Workflow

A workflow of heterogeneous velocity inversion and MS location is shown in Fig. 2. The workflow consists of four steps: drilling and blasting signal analysis, surface wave dispersion inversion, adjoint-state traveling time tomography, and L2 norm double-difference location. The absolute arrival time of the P-wave and S-wave can be extracted from the processed drilling and blasting source signals. The dispersion inversion provides an estimated layered S-wave velocity of the monitoring area, indicating the development of the EDZ and geological setting in the depth direction (y-axis in Fig. 1). The blasting starting time t_0 can be determined by wave backward propagation analysis using the known location of the source and sensors, arrival time of the S-wave and inverted S-wave velocity model. Then, the absolute traveling time of the P-wave can be calculated, because the t_0 values of the S-wave and P-wave are consistent. Traveling time tomography using multiple drilling and blasting source images is used to create a heterogenous P-wave velocity model between sources and sensors. More sources can be taken into account with deeper drilling. Double-difference location is conducted using the P-wave arrival time and the last inverted P-wave heterogeneous velocity model. The four steps of the workflow are described as follows:

a.   Drilling and blasting signal analysis
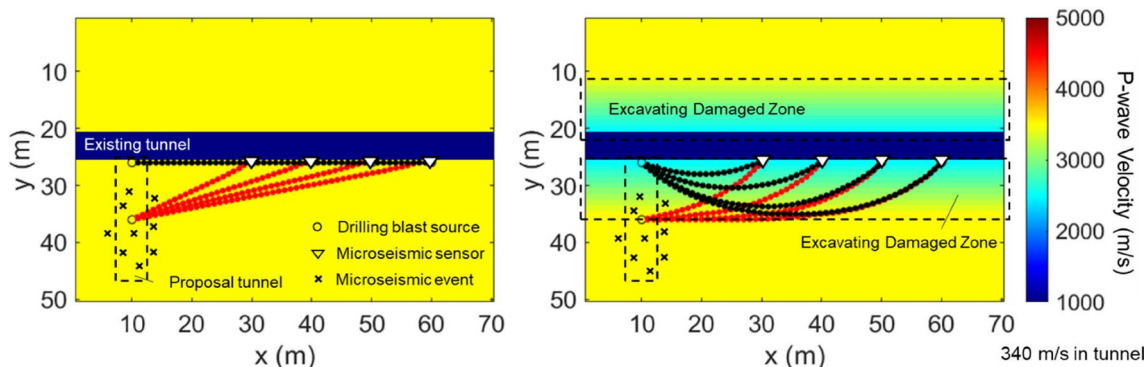

Fig. 1 Influence of the heterogeneous velocity on wave propagation (taking the EDZ of the tunnel as an example): wave propagation paths in **a** homogeneous velocity model and **b** heterogeneous velocity model
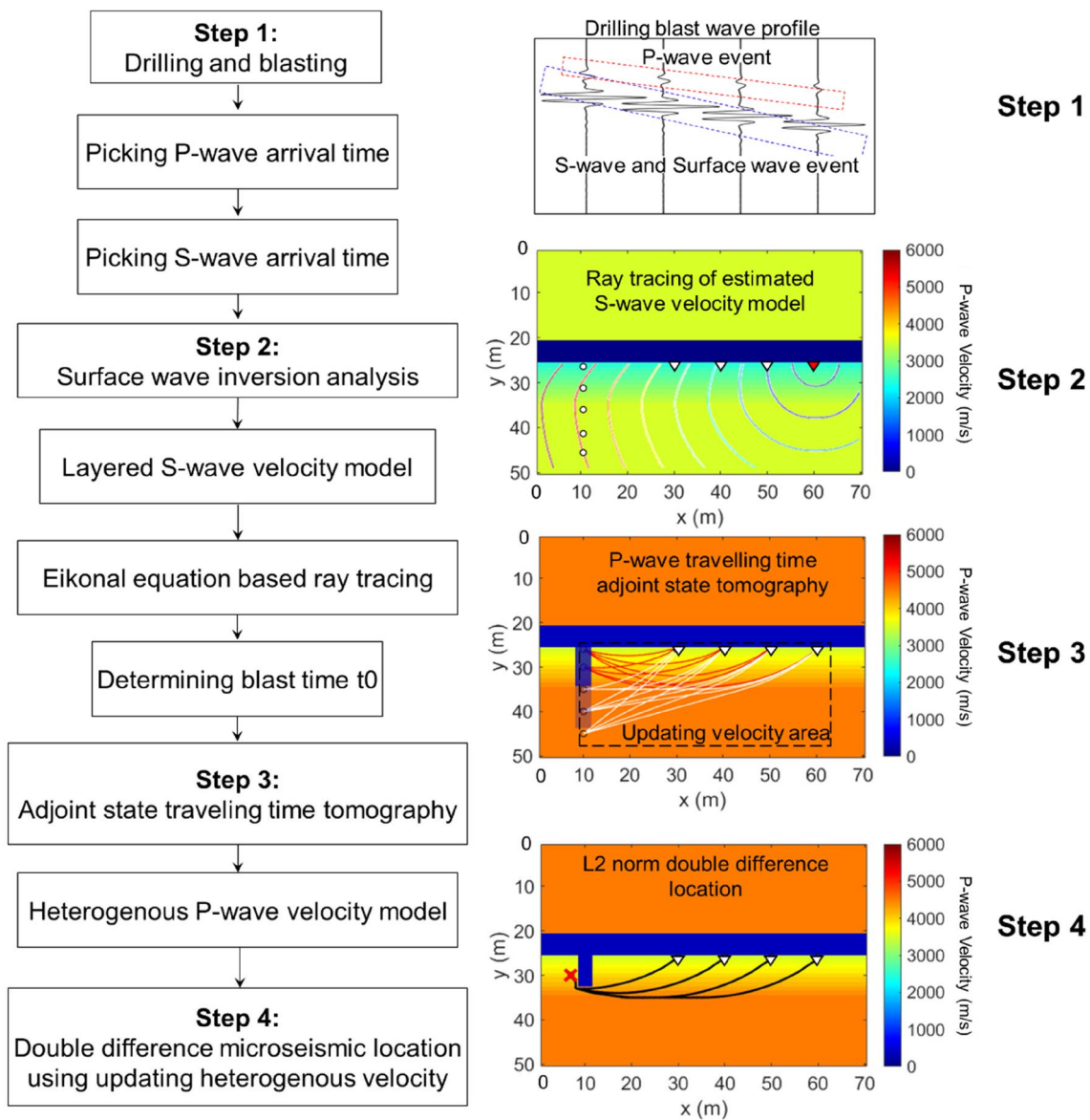
Fig. 2 Overall workflow of MS source location in a deep tunnel using heterogeneous velocity updating

The bandpass filter is deployed to remove the background noise and enhance the signal-to-noise ratio. The drilling blast wave profile is shown in Fig. 2. The P-wave and S-wave signals can be identified based on the slope corresponding to the events. The drilling blast source in the actual project is a long signal of several seconds due to multiple blasting events. We analyze the signal of the first blast only because of its clean first arrival time without any overlap. The accurate pick of the P-wave is more straightforward than that of the S-wave. It is difficult to identify the S-wave arrival due to the interference of the P-wave (e.g., the left trace in the scheme figure of step 1). However, the S-wave and P-wave gradually separate as the offset increases. The arrival time of the S-wave at the most significant offset is used to estimate t_0 in the next step.

b. Surface wave inversion analysis

Dispersion inversion of the surface wave is applied to reconstruct the S-wave velocity model, so that t_0 can be calculated by ray backward tracing, as shown in step 2 in Fig. 2. The dispersion curve is extracted from the processed drilling blast wave profiles by the phase-shift method (Park et al. 1998). The initial model is a linearly increasing velocity S-wave model. The 1D

S-wave velocity profile can be obtained by iteration to fit the observed and simulated dispersion curves. The S-wave velocity profile in step 2 describes the EDZ range. Note that t_0 is not needed during surface wave dispersion inversion. Thus, it is possible to calculate t_0 by an inverted S-wave model and the S-wave arrival time and location of the source and sensors. Ray tracing can be conducted on the inverted S-wave by solving the eikonal equation using the FMM. The contour of traveling time from the sensor (red triangle at the right in step 2 scheme) is also shown in the figure. Thus, the backpropagating traveling time can be obtained and used to calculate t_0 as Eq. (1):

$$t_0 = t_s - t_b, \tag{1}$$

where t_s is the arrival time S-wave recorded by the sensor with the largest offset and t_b is the corresponding backpropagating traveling time from the sensor to the blasting source. The parameter t_0 of the blasting source at different depths can be calculated similarly.

   c. Adjoint-state traveling time tomography

      After obtaining t_0 of the blasting source, the absolute traveling time of the P-wave can be calculated. First-arrival traveltime tomography using the adjoint-state method is developed to invert the P-wave velocity model. The high-density ray path gradually covers the monitoring area when multiple blasting sources are included in the tomography (scheme of step 3 in Fig. 2). The P-wave velocity within the ray path coverage is updated during the tomography iteration. The initial P-wave velocity model can be estimated based on the S-wave profile. The P-wave velocity model is updated until the misfit between the observed and simulated traveltimes converges. An adjoint-state parameter is introduced during the inversion to speed up the iteration. Tomography can be conducted after every drilling and blasting, which updates the P-wave velocity model using the newly added blasting source signal. Thus, a constantly updated heterogenous P-wave velocity can be obtained during tunneling.d. Double-difference MS location using updating the heterogenous velocity model

A heterogeneous P-wave velocity model is used to locate the source of MS during tunneling. During the location of the MS, an arrival time difference between two sensors of one event is measured as Eq. (2):

$$r_{ij}^k = \left(t_i^k - t_j^k\right)^{\text{obs}} - \left(t_i^k - t_j^k\right)^{\text{cal}}, \tag{2}$$

where r_{ij}^k is the arrival time difference between sensors i and j ($i, j = 1,2 \ldots n$, n is the total number of sensors) for MS event k. Obs and Cal are the observed and calculated values of the arrival time, respectively. The FMM (Kroon 2021) is applied to model the travel time using an updating heterogenous velocity model. Thus, the objective function of location for MS event k can be established as an L2 norm of the arrival time difference:

$$F(x, y) = \sum_{i=1, j=2}^{n} \left(\left(t_i^k - t_j^k\right)^{\text{obs}} - \left(t_i^k - t_j^k\right)^{\text{cal}} \right)^2, \tag{3}$$

where (x, y) is the location of the MS source. The simplex method (Nelder and Mead 1965; Li et al. 2014) is used to minimize the objective function [Eq. (3)]. The simplex method searches the MS source's location by moving and distorting the simplex shape to converge to the lowest misfit.

The proposed MS source location algorithm to invert updating heterogeneous velocity models using blasting seismic data. The surface wave inversion is used to consider the effect of the EDZ. The FMM is used to calculate the traveling time and ray tracing and estimate the t0 of the blasting source. Traveling time tomography is then conducted to obtain a heterogeneous P-wave velocity model. More blasting sources are added to the tomography with drilling construction going on. Finally, the MS location can be determined based on the double-difference objective function and the simplex method. The details of surface wave inversion analysis, adjoint-state traveling time tomography and double-difference MS location algorithms are described as follows:

2.3 Surface Wave Inversion

In the surface wave inversion, the phase-shift method (Park et al. 1998) is applied to extract the dispersion curve from the drilling blast wave profile. Then, we introduce an improved perturbational inversion of the fundamental mode of the Rayleigh wave dispersion curve (Liu and Wang 2021) to invert a layered S-wave velocity model. The improved perturbational inversion consists of two parts: the modified TLM forward simulation and perturbational inversion.

The modified TLM forward simulation first builds a matric function (Kausel and Roësset 1981):

$$\boldsymbol{K} = k^2 \boldsymbol{B}_2 + k \boldsymbol{B}_1 + \boldsymbol{B}_0 - \omega^2 \boldsymbol{M} \tag{4}$$

where k is the wavenumber and ω is the angular frequency of excitation. The stiffness matrices $\boldsymbol{B}_0$, $\boldsymbol{B}_1$, and $\boldsymbol{B}_2$ are matrix functions of Lame's first parameter and shear modulus, whereas the mass matrix $\boldsymbol{M}$ depends only on the density. The problem of $\boldsymbol{Det}(\boldsymbol{K}) = 0$ becomes a typical generalized quadratic eigenvalue problem in terms of wavenumber k:

$$(k^2 B_2 + kB_1 + B_0)v = \omega^2 M v \tag{5}$$

which can be solved using the root-searching method (HE et al. 2006) to obtain the eigenvalue k and the eigenvector v. An eigenvalue k and its corresponding eigenvector v are together called an eigenpair. For a fixed frequency ω, multiple eigenpairs can often be obtained. The eigenvector v represents a mode shape, and the eigenvalue k (together with ω) represents the Rayleigh wave phase velocity $V_R = \frac{\omega}{k}$. In the modified TLM, we use inverse iteration (Moler and Stewart 1973) to compute the eigenvector v_j corresponding to (ω_j, V_{Rj}) for $j = 1, 2, \ldots, m$ and complete the forward simulation.

The perturbational inversion method updates the model $m = (V_s, V_p, \rho)$ by solving the optimization problem:

$$J(m)\Delta m = \Delta b, \tag{6}$$

where Δb, a function of the frequency ω, is the difference between the observed and simulated dispersion curves. $\boldsymbol{J(m)}$ is a Jacobian matrix calculated based on the Haney and Tsai (2017) formula:

$$J(m) = \frac{\delta V_R}{\delta V_s}. \tag{7}$$

To solve the optimization problem, we define a weighting matrix W depending on the absolute difference in the Rayleigh wave velocity with respect to frequency as

$$W = L^T L, L = \mathrm{Diag}\left(\frac{|\Delta b|}{\Delta b_{\inf}}\right), \tag{8}$$

where $|\Delta b|$ is the absolute of column vector Δb, $|\Delta b|_{\inf}$ is the maximum element of $|\Delta b|$, and L is a diagonal matrix whose diagonal terms consist of $\frac{|\Delta b|}{|\Delta b|_{inf}}$. We apply this weighting matrix to Eq. (5) to obtain

$$A(m)\Delta m = d, \tag{9}$$

where $A(m) = L * J(m)$ and $d = L * \Delta b$. During an iterative optimization process $A_k(m_k)\Delta x_k = d_k, k = 1, 2, \ldots, \mathrm{iter\_max}$, we calculate the least-square solution Δx_k for the kth iteration and update the model by

$$m_{k+1} = m_k + \Delta m. \tag{10}$$

Upon obtaining the S-wave velocity model by surface wave inversion, the FMM (Kroon 2021) is introduced to calculate the S-wave travel time from the sensors to the blasting source and estimate t_0 of the blasting source by Eq. (1).

2.4 Adjoint-State Eikonal Equation Tomography in Deep Tunnels

The P-wave traveling time can be calculated based on the t_0 of the blasting source and the arrival time of the P-wave. The objective misfit function of P-wave traveltime tomography in a deep tunnel can be established as

$$E(c) = \frac{1}{2} \int_{\partial\Omega} \left[T(c,r) - T^{\mathrm{obs}}(r)\right]^2 \mathrm{d}r \tag{11}$$

in which observed traveltimes $T^{\mathrm{obs}}(r)$ are picked from the test data and r represents the sensors at the designed monitoring acquisition surface $\partial\Omega$. $T(c,r)$ is the modeled traveltime obtained by solving the eikonal equation for model velocity c:

$$F(t,c) = [\nabla t(x)]^2 - \frac{1}{c^2(x)} = 0, \tag{12}$$

where x is any point between the blasting sources and sensors Ω and where $t\,(x_{\mathrm{soure}})$ is equal to zero. The eikonal equation can be solved by the FMM (Kroon 2021). In the classic approach, the objective function can be expanded at c_0 by employing the Gaussian expansion method:

$$E(c) \approx E(c_0) + \left[\frac{\partial E(c)}{\partial c}\Big|_{c=c_0}\right]^T \delta c + \frac{1}{2}\delta c^T \frac{\partial^2 E(c)}{\partial c\partial c^T}\Big|_{c=c_0} \delta c. \tag{13}$$

The gradient can be defined as the first derivative of the objective function relative to the velocity of medium c. The Hessian matrix is the second derivative, as shown in Eq. (13):

$$g = \frac{\partial E(c)}{\partial c}, \tag{14}$$

$$H = \frac{\partial^2 E(c)}{\partial c\partial c^T}. \tag{15}$$

To obtain the minimum of the objective function, we set $g = 0$ to obtain

$$H|_{c0}\delta c = -g|_{c0}, \tag{16}$$

$$\delta c = -(H|_{c0})^{-1} g|_{c0}. \tag{17}$$

The updated model can be written as

$$c_{n+1} = c_n - (H|_{cn})^{-1} g|_{cn}. \tag{18}$$

The updated model parameter c_{n+1} is used as the initial model in the next iteration. However, it is difficult to compute the inverse of Hessian matrix $\boldsymbol{H}$ and Fréchet matrix g. The adjoint-state method is introduced to compute the

gradient of the misfit function without introducing Fréchet derivatives. The Lagrangian formulation is added to the objective misfit function [Eq. (10)]. The extended objective function is

$$L(c, t, \lambda) = \frac{1}{2} \int_{\partial\Omega} \left[t(r) - T^{obs}(r)\right]^2 \mathrm{d}r - \frac{1}{2} \int_{\Omega} \lambda(x)[\nabla t(x)]^2 - \frac{1}{c^2(x)} \mathrm{d}\Omega,$$

(19)

where $t(r)$ is the solution of the eikonal equation at receiver x and where $\lambda(x)$ is the Lagrangian multiplier and is named the adjoint-state parameter, which can ensure that $t(r)$ equals T^{obs} at the optimum. When searching for the minimum of the objective, the traveltime $t(r)$, Lagrangian multiplier $\lambda(x)$, and velocity $c(x)$ are independent. When the objective function reaches the minimum value, the variable satisfies Eqs. (20), (21) and (22):

$$\frac{\partial L}{\partial \lambda} = 0,$$

(20)

$$\frac{\partial L}{\partial t} = 0,$$

(21)

$$\frac{\partial L}{\partial c} = -\int_{\Omega} \frac{\lambda}{c^3(x)} \mathrm{d}x = \frac{\partial E}{\partial c}.$$

(22)

According to Eq. (21), we have

$$\frac{\partial L}{\partial t} = \int_{\partial\Omega} \left[t(r) - T^{obs}(r)\right]\mathrm{d}r - \int_{\Omega} \lambda(x)\nabla t(x)\frac{\partial \nabla t}{\partial t}\mathrm{d}x = 0,$$

(23)

We apply the Gauss formula to the second term of Eq. (23):

$$\frac{\partial L}{\partial t} = \int_{\partial\Omega} \left[t(r) - T^{obs}(r) - \lambda n\nabla t\right]\mathrm{d}r + \int_{\Omega} \nabla \lambda(x) \cdot \nabla T(x)\mathrm{d}x = 0.$$

(24)

Two integral terms are set to zero in Eq. (23). Thus, λ is the solution of

$$\nabla \cdot (-\lambda \nabla T) = 0 \quad \text{between the sources and sensors} \quad (25)$$

with boundary condition

$$(n \cdot \nabla T)\lambda = T(r) - T^{obs}(r) \quad \text{in the tunnels.} \quad (26)$$

The FSM (Taillandier et al. 2009) is used to calculate λ in Eq. (25) over the whole model with the boundary condition of Eq. (26). Thus, the gradient $\frac{\partial E}{\partial c}$ can be obtained by Eq. (22). The model update is as follows:

$$c_{n+1} = c_n + \alpha\frac{\partial E}{\partial c},$$

(27)

where α is the step length. The inversion iteration is stopped when the objective function is less than a given threshold.

2.5　MS Source Location Using the Heterogeneous Velocity

The objective function of the MS source location in deep tunnels is established as Eq. (2) using the L2 norm double traveling time difference. When searching the location, the forward modeled traveling time is calculated by the FMM using the inverted heterogeneous P-wave velocity model. The simplex method is introduced as a nonlinear optimization technique to speed up the search for the minimums of the objective function. The simplex method creates an $N + 1$ dimensional simplex in an objective function value space to search for a minimum in an N-dimensional space. The lower value point replaces the high-value point by reflection, expansion, contraction and shrinkage (Li et al. 2014) until the minimum is reached.

Note that inverted heterogenous velocity models are 2D due to the tunnel construction's linear monitoring acquisition geometry. The starting time of the source is not cancelled in the double-difference objective function. Thus, a simplex geometry for a 2D space is a triangle. The workflow of the double-difference source location method based on the simplex method can be concluded as:

a.　Establish a double-difference source location objective function as Eq. (2). Three points P_1, P_2 and P_3 are selected as an initial simplex triangle based on the MS monitoring area.

b.　Calculate the three objective function values corresponding to three points P_1, P_2 and P_3 as y_1, y_2 and y_3 using the FMM of the current inverted heterogeneous velocity model. Define y_{min}, y_{mid} and y_{max} as the minimum and maximum of y_1, y_2 and y_3 and the corresponding minimum and maximum points as P_{min}, P_{mid} and P_{max}, respectively. The reflection, expanding, and contracting points and corresponding values are defined as P^*, P^{**}, P^{***} and y^*, y^{**}, y^{***}, respectively.

c.　Start the searching iteration. The reflection point P^* is searched, and the corresponding objective function value y^* is calculated and compared to y_s and y_m. Then, a new simplex can be determined based on the principle of four transformations (i.e., reflection, expansion, contraction and shrinkage), as shown in Fig. 3. The formula and details of transformation can be found in Li et al. (2014).

d.　Repeat steps (b)–(c) until the misfits are lower than the threshold and the best fit location has been found.

e.　Repeat steps (a)–(d) when more blasting sources are added to the travel tomography to obtain a new heterogeneous P-wave velocity model.
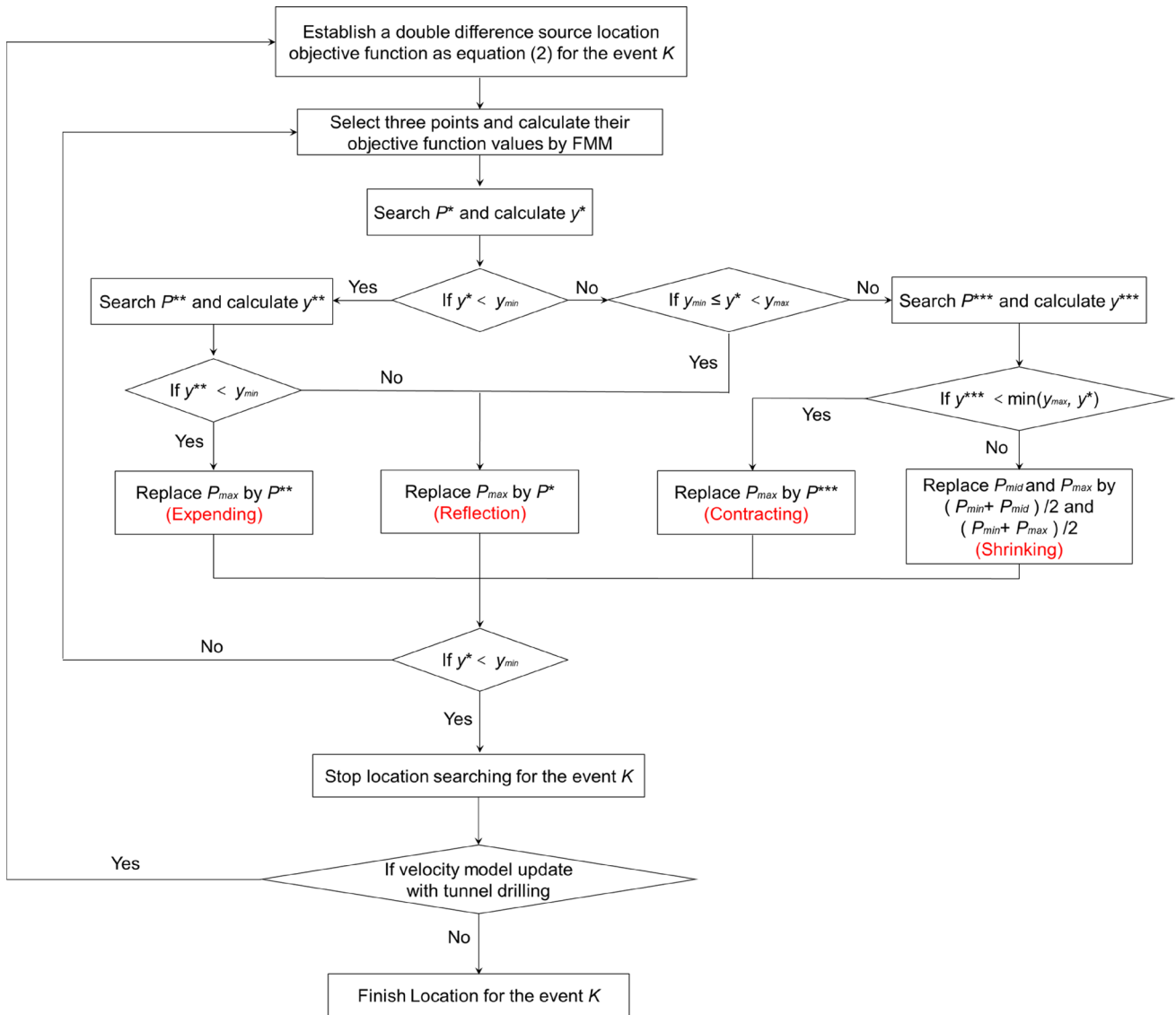
Fig. 3 Workflow of double-difference simplex-based MS source location

3 Numerical Study

The numerical simulation of a realistic deep tunnel model illustrates the proposed inversion method of the heterogenous velocity model. We present wave field snapshots to feature the characteristics of P-wave, S-wave and surface wave propagation in tunnels. Blasting seismic data are used to invert the velocity model considering the effect of the EDZ. Multiple MS events around the drilling tunnels are located to evaluate the accuracy of the proposed MS source location method.
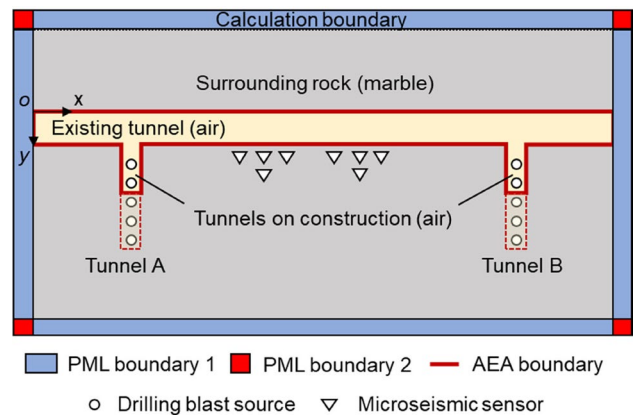

Fig. 4 Scheme of the MS source location numerical simulation model

3.1 Numerical Modeling of the Blasting Source

Figure 4 shows the numerical model, including an existing tunnel and two new tunnels in construction that are vertical to the existing tunnel. A convolutional perfectly matched layer (CPML) boundary is assigned at the boundary of the computing domain, which can absorb the reflection from the computed boundary. Thus, the wave propagation simulation can be conducted in a defined domain. The acoustic–elastic boundary approach (AEA) (Xu et al. 2007) is applied to address the free (air) boundary. We implement the high-order FDTD to solve the viscoelastic wave equation. The generalized standard linear solid (GSLS) method (Bohlen 2002) considers the attenuation and dispersion of viscoelastic waves. The stress–velocity formulation of the viscoelastic waves based on GSLS are shown as

$$\rho \frac{\partial v_i}{\partial t} = \frac{\partial \sigma_{ij}}{\partial x_j} + f_i, \tag{28}$$

$$\frac{\partial \sigma_{ij}}{\partial t} = \frac{\partial v_k}{\partial x_k} \{\pi(1 + \tau^P) - 2\mu(1 + \tau^s)\} \\ + 2\frac{\partial v_i}{\partial x_j}\mu(1 + \tau^s) + \sum_{l=1}^{L} r_{ijl} \quad \text{if} \quad i = j, \tag{29}$$

$$\frac{\partial \sigma_{ij}}{\partial t} = \left(\frac{\partial v_k}{\partial x_k} + \frac{\partial v_k}{\partial x_k}\right)\mu(1 + \tau^s) + \sum_{l=1}^{L} r_{ijl} \quad \text{if} \quad i \neq j, \tag{30}$$

where σ_{ij} denotes the ijth component of the stress tensor, v_i are the components of the particle velocities. f_i are the components of the external body force. τ^p and τ^s are the levels of attenuation for P- and S-waves, respectively, which are related to the seismic quality factors Q_p and Q_s, respectively.

The two new tunnels are alternately drilled, as shown in Fig. 4. The model measures 100 m in width × 50 m in depth with a 0.2 m spatial interval in both x- and y-directions. The starting points (x, z) of tunnels A and B (the middle point of the drilling face) are (15,0) and (85, 0), respectively. The MS monitoring network is installed in the middle of the
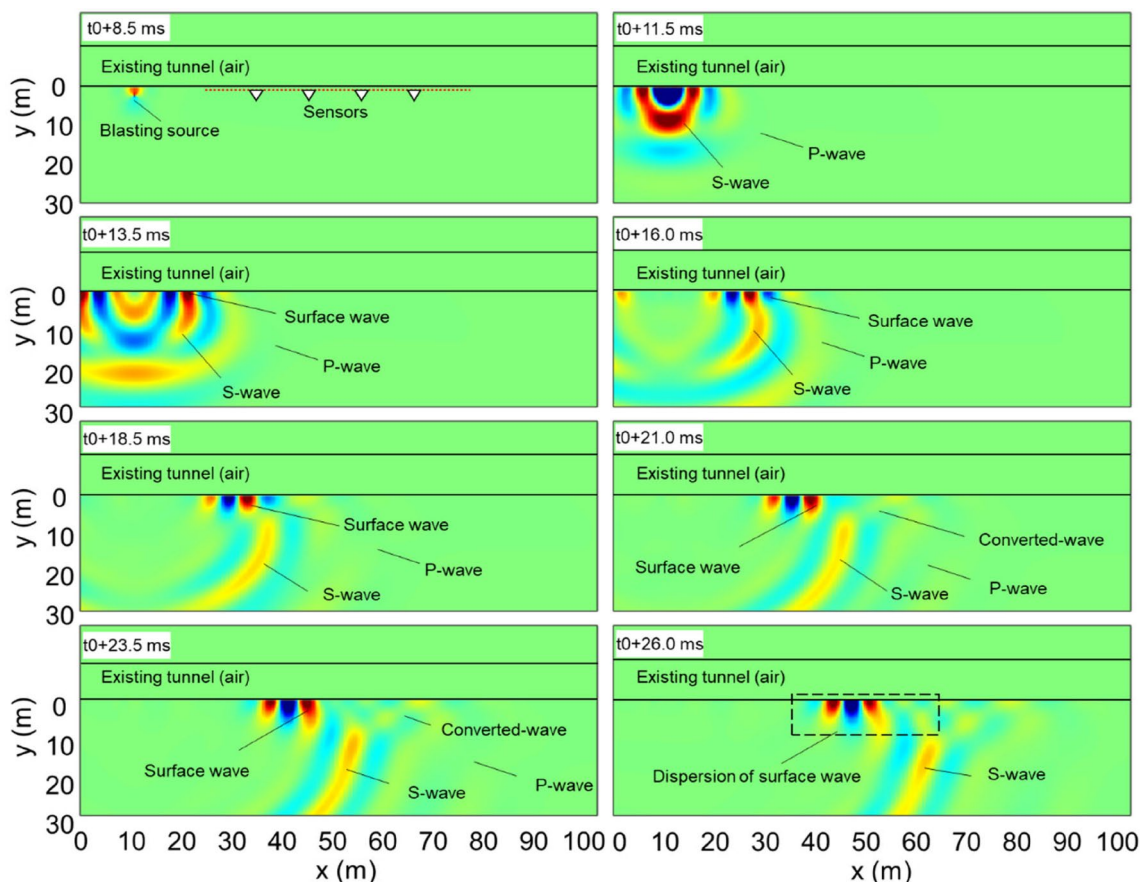

Fig. 5 Snapshots of the first blasting source at tunnel A

two new tunnels, consisting of 8 sensors located at (35, 1), (40, 1), (40, 4), (45, 1), (55, 1), (60, 1), (60, 4) and (65, 1). The drilling and blasting sources are set at the middle axis of tunnel drilling every 2 m. The blasting source wavelet is a Ricker wavelet with a dominant frequency of 120 Hz. The background (surrounding rock) S-wave, P-wave velocity and density are 3500 km/s, 5250 km/s and 2.5 g/cm^3, respectively. The S-wave velocity varies from 3500 m/s to 2500 m/s in the zone of 10 m around the tunnel (i.e., EDZ). The ratio of the P-wave and S-wave velocities is 1.5 in the EDZ zone. The total simulation time length is 50 ms with a sampling interval of 0.02 ms.

Snapshots of the first blasting source are shown in Fig. 5. The Ricker wavelet is transmitted at the middle axis of tunnel A as a blasting source. The P-wave and S-wave gradually separate due to the velocity difference. The surface wave (Rayleigh wave) traveling along the sidewall of the tunnel can be observed after $t_0 + 13.5$ ms. The propagation of the surface wave is slightly slower than that of the S-wave, since the velocity of the surface wave is typically 0.9 times that of the S-wave. The P–S converted wave, which can be seen in the snapshot of $t_0 + 21.0$ ms, is caused by the P-wave reflected at the sidewall of the tunnel. The S-wave travels with a higher velocity in the deeper area in the y-direction, because the S-wave velocity of intact rock is higher than that in the EDZ zone. The dispersion of the surface wave can be observed at $t_0 + 13.5$ ms. The surface wave with different frequencies travels along the sidewall with different velocities.

Figure 6 presents the vertical velocity component of four sensors at (35, 1), (45, 1), (55, 1) and (65, 1) and their corresponding frequency spectrum. Note that t_0 is an unknown parameter in most drilling and blasting tunneling cases. Thus, t_0 in the time axis in Figs. 5 and 6a is to be determined. The P-wave, S-wave and surface wave events can be identified based on the different slopes of the events. The arrival time of the P-wave and S-wave can be extracted as the blue and red lines in Fig. 6a. The accurate arrival time of the P-wave can be easily determined for every trace. However, the single arrival time of the S-wave of the no. 4 sensor can be identified directly. The overlap influences the identification of the arrival time of the S-wave of sensor nos. 1, 2 and 3. The dispersion of the surface wave can be observed from the more extended events in the farther offset recordings. The dominant frequency of recordings varies from 150 to 170 Hz (Fig. 6b), consistent with the actual blasting source signal in tunnels.

3.2 Determining t_0 of the Blasting Source

The phase-shift method (Park et al. 1998) is used to calculate the four recordings' dispersion curves. The dispersion curve calculated by four recordings is shown in Fig. 7a. The limited number of sensors causes spatial aliasing, as shown in Fig. 7a. The dispersion curve is calculated by 11 assuming sensors located from (25, 1) to (75, 1) with the same spacing, as shown in Fig. 7b. The dispersion curves of the fundamental mode in Fig. 7a, b are the same, and the dispersion curve energy is consistent with the theoretical solutions (white stars in Fig. 7). The comparison demonstrates that the surface wave modeling is correct, and the dispersion curve of the fundamental mode can be extracted by the four linear monitoring sensors.
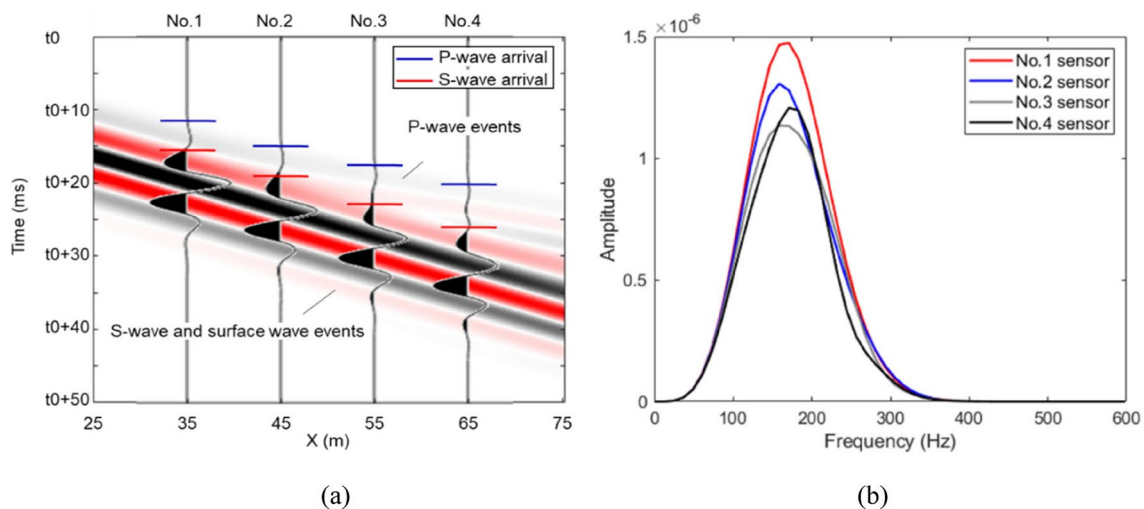

(a)

(b)

Fig. 6 Simulated recordings of four sensors at the (35, 1), (45, 1), (55, 1) and (65, 1) **a** wave profiles and **b** corresponding frequency spectra
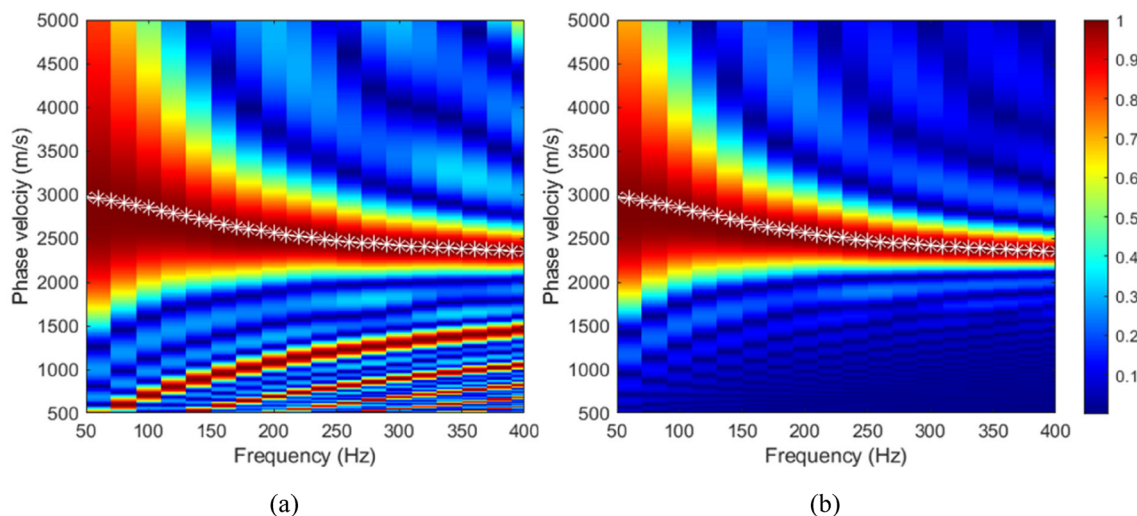
Fig. 7 Dispersion curve of blasting source recordings. **a** Dispersion curve calculated by four recordings. **b** Dispersion curve calculated by the recordings of simulated sensors along the red dashed line in Fig. 5. White stars are the theoretical dispersion curve solutions
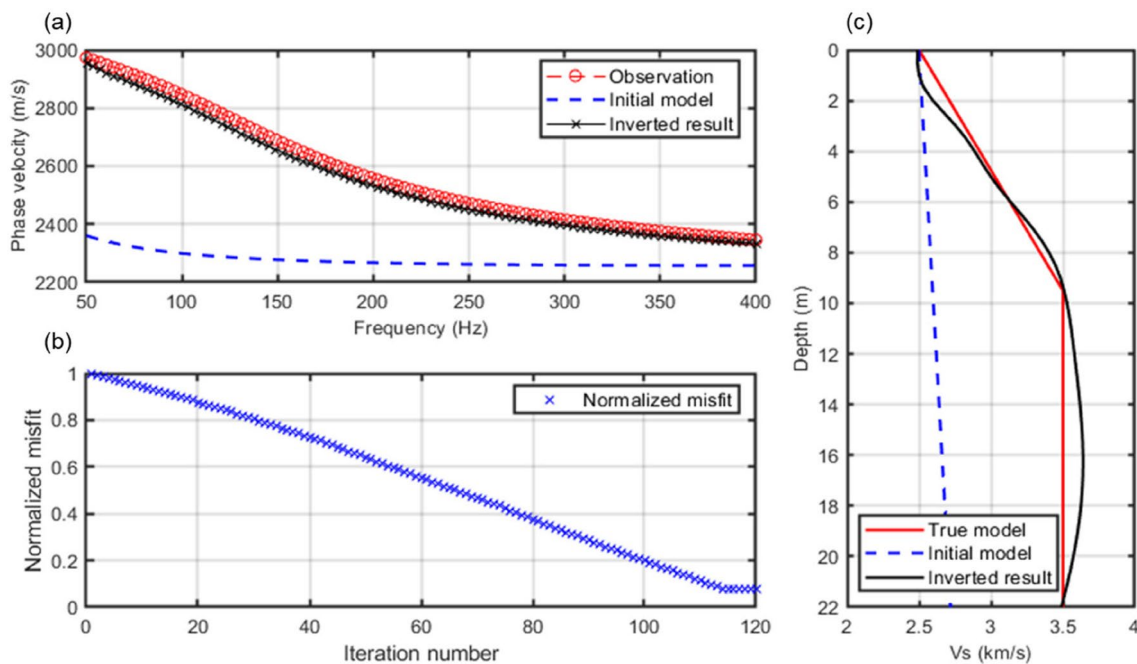

Fig. 8 Inversion process of the dispersion curve using the improved perturbational inversion method: **a** dispersion curve comparison at the 120th iteration; **b** misfit evolution; and **c** S-wave velocity comparison at the 120th iteration

We use the proposed improved perturbational inversion met hod to invert the dispersion curve extracted from Fig. 7a. The process of the inversion is shown in Fig. 8. The initial S-wave velocity model varies from 2500 to 2700 m/s (the blue dashed line in Fig. 8c). The corresponding dispersion of the initial model is shown in Fig. 8a. A significant difference between the observed and initial dispersion curves can be seen. The inversion aims to narrow the misfits of the dispersion curve by updating the S-wave velocity model. The ratio of the P- and S-wave velocities is 1.5, and the density is constant during the whole inversion. The misfits rapidly decrease, as shown in Fig. 8b. After the 120th iteration, the misfit curve converges to a 0.14 normalized misfit and stops updating. The inverted S-wave presents a low-velocity zone in the depth range from the surface to 10 m, which is consistent with the preset true S-wave velocity model.

Fig. 9 Backpropagation of the S-wave from sensor no. 4 to the first blasting source at tunnel A: **a** ray tracing based on the inverted S-wave velocity model and **b** ray tracing based on the homogeneous S-wave velocity model
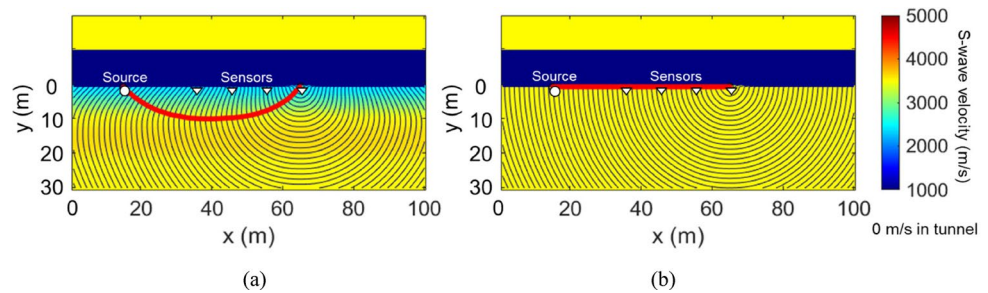
Table 1 Calculation of the drilling blast source t_0 of the numerical study

Number of sensors	Arrival time t_s of S-wave (ms)	Calculated travelling time t_b of actual S-wave velocity model (ms)	Calculated travelling time t_b of inverted S-wave velocity model (ms)	Calculated travelling time t_b by homogenous S-wave velocity model (ms)	Calculated t_0 of actual S-wave velocity model (ms)	Calculated t_0 of inverted S-wave velocity model (ms)	Calculated t_0 of homogenous S-wave velocity model (ms)
No.1 sensor	15.86	7.80	8.01	5.71	8.06	7.85	10.15
No.2 sensor	19.31	11.27	11.59	8.57	8.04	7.72	10.74
No.3 sensor	22.42	14.40	14.63	11.43	8.02	7.79	10.99
No.4 sensor	25.33	17.29	17.50	14.28	8.04	7.83	11.05
Average	–	–	–	–	8.04	7.79	10.7

Meanwhile, the dispersion curve of the final results fits the observation well.

The inverted S-wave layered model is established in Fig. 9a. The contour lines calculated by the FMM in Fig. 9a are the isochrones, which are curves of equal travel time. The ray tracing of backpropagation from the sensor to the source is calculated by searching the normal direction of every contour line. The ray tracing results show that the wave propagation path is significantly different between the inverted S-wave and homogenous models. The EDZ zone of low velocity deepens the curve of wave path travel, while the wave path in the homogeneous model is a line. The traveling time of the S-wave can be obtained from the contour lines, as shown in Table 1. The travel times from the four sensors to the source are calculated based on actual, inverted, and homogeneous models. The travel times t_b calculated by the inverted and actual models are similar. However, the traveling time t_b calculated by the homogeneous model is much shorter due to the lack of consideration of the EDZ. The parameter t_0 is calculated according to the S-wave arrival time and Eq. (2). As shown in Table 1, the error of t0 identified by the inverted S-wave model is approximately 0.2 ms, much less than the error (2–3 ms) calculated by the homogenous model. Thus, t_0 estimated by the inverted S-wave model can be regarded as the trigger time of the blasting source.

3.3 P-Wave Traveling Time Tomography While Drilling

The P-wave traveling time tomography can be conducted after the blasting source trigger time t_0. The absolute traveling time of the P-wave can be calculated by the blasting source t_0 and selected arrival time of the P-wave (e.g., the blue line in Fig. 6a). The simulated blasting source is set in the middle lines of the two tunnels with a 2 m interval. Eight sensors between the two tunnels are used to obtain the travel time and invert the P-wave velocity. The results of P-wave traveling time tomography during drilling are shown in Fig. 10. Figure 10a presents the true P-wave velocity model, which overlays the low-velocity zone (i.e., the EDZ) of the existing tunnel and two new tunnels. The surrounding rock away from the tunnel sidewall has a higher P-wave velocity. The initial model is estimated by the inverted S-wave velocity model. Four traveling time tomography are conducted by the proposed adjoint-state method when the tunnels are drilled to 5 m, 10 m, 14 m, and 18 m, respectively.

The inverted P-wave velocity model gradually updates to the true model, as shown in Fig. 10c–f. In the first drilling step (2 m in depth, Fig. 10c), the major update of the velocity model is at the near field of the existing tunnel, which the ray path of the first three blasting waves mainly covers. The inverted P-wave models (Fig. 10c–f) are almost symmetric
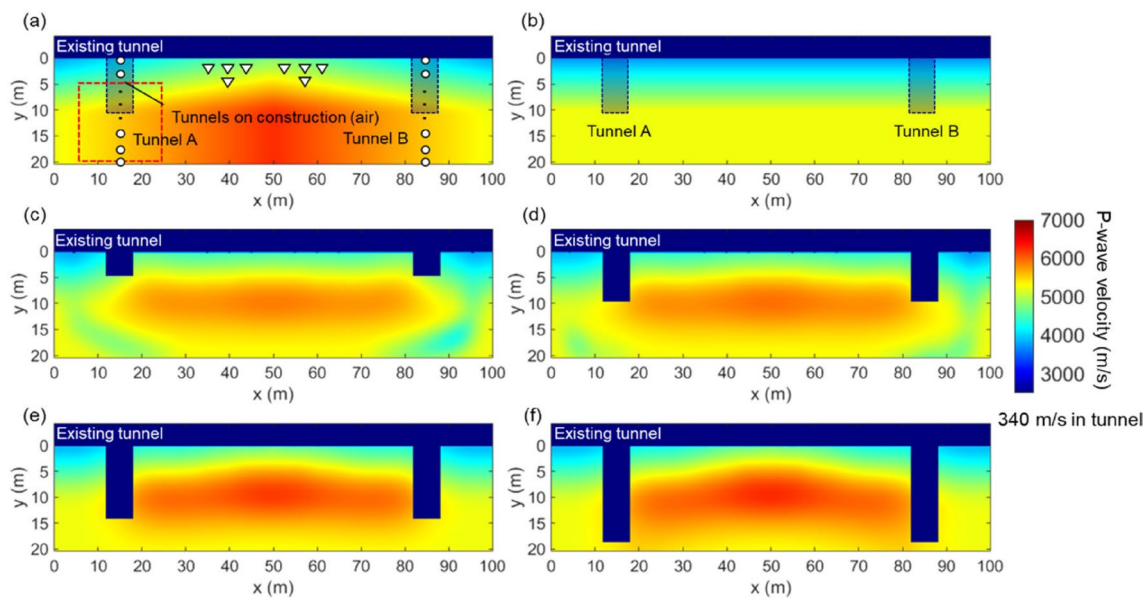
Fig. 10 Results of P-wave traveling time tomography during drilling: **a** true model; **b** initial model; **c–f** P-wave tomography when two tunnels are drilled to depths of 5 m, 10 m, 14 m and 18 m, respectively

Fig. 11 Inverted P-wave velocity comparison: **a** x = 20 m, **b** x = 30 m, **c** x = 40 m, and **d** x = 50 m
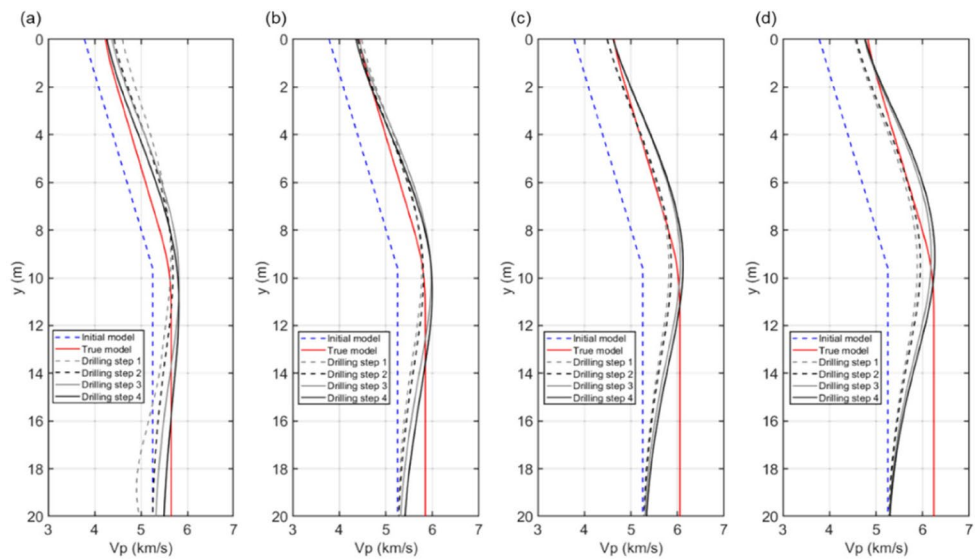
due to the symmetry monitoring setup and true velocity model. The velocity model in Fig. 10d has a similar distribution, but the velocity value is still visibly different from the true model. The inverted models of steps 3 and 4 (Fig. 10e, f) are highly consistent with the true model. The details of the velocity comparison are shown in Fig. 11. The velocity logs of the inverted, true and initial models at x = 20, 30, 40 and 50 m demonstrate that the P-wave traveling time tomography effectively obtains reasonable heterogeneous models while drilling. In general, the inverted P-wave velocity is closer to the true value with the addition of blasting sources. The middle of the monitoring area (around x = 50, y > 12 m) presents a more significant error due to the lack of ray path travel. However, those misfits do not affect the accuracy of the location for the MS source, since the wave of the MS event around the tunnel also does not travel through that area to the sensors.

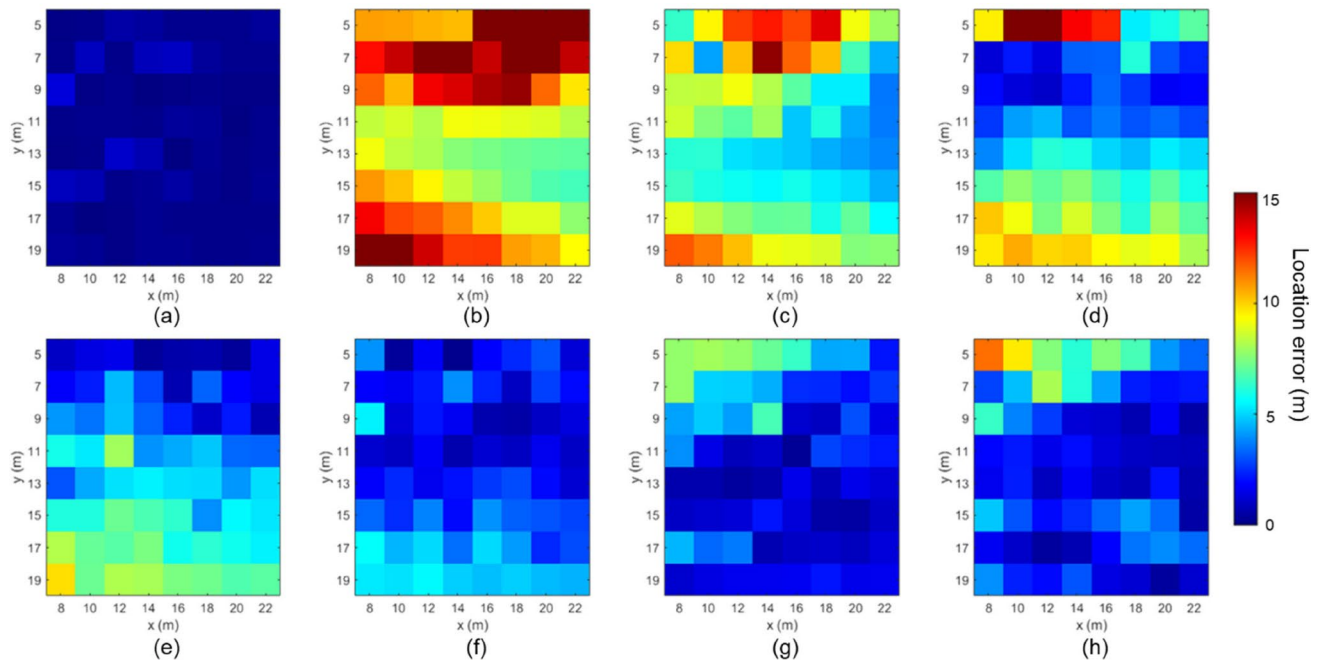**Fig. 12** Location errors of the MS source within the red dashed square in Fig. 10a using different P-wave velocity models. **a** True model. **b** Homogeneous model of 4500 m/s. **c** Homogeneous model of 5000 m/s. **d** Homogeneous model of 5500 m/s. **e** Inverted model of step 1 (Fig. 10c). **f** Inverted model of step 2 (Fig. 10d). **g** Inverted model of step 3 (Fig. 10e). **h** Inverted model of step 4 (Fig. 10f)

3.4 MS Source Location

Sixty-four (8×8) MS sources that are uniformly distributed in the red square in Fig. 10a (ranging from 5 to 19 m on the X-axis and 8–22 m on the Y-axis) are used to test the location accuracy using different velocity models. The forward-simulated arrival time is calculated using the eikonal equation based on the FMM. The location results for all the MS sources can be found in Appendix Tab le 4. The location errors using different homogenous velocity models and inverted velocity models of different steps are shown in Fig. 12. Figure 12a shows the location error using the true model, which means that there is no error in the location velocity model. The location error in Fig. 12 is small and consistent, which demonstrates the accuracy of the double-difference simplex location method. Thus, when we conduct location using the inverted and homogenous velocity models, the errors are generally caused by the velocity model difference.

The location results of the homogenous velocity (4500, 5000, 5500 m/s) models present significant errors (Fig. 12b, c, d). The location accuracy is primarily affected by the velocity difference between the homogeneous and true velocity models, especially the velocity difference in the EDZ zone. The location at a depth of 9 m using a model velocity of 5500 m/s presents a smaller error, because 5500 m/s is close to the average velocity at that depth. However, the location error dramatically increases at other depths due to the heterogeneity of the true model velocity.

Note that the location accuracy improves using updating inverted velocity models (Fig. 12e–h). The location presents a high accuracy around the depth of the current drilling face. For example, the tomography for the traveling time uses blasting sources with drilling depths of less than 5 m, 10 m, 14 m and 18 m. Thus, the location using four inverted velocities fits the true location of MS events near the drilling face well (referring to 5 m, 10 m, 14 m and 18 m in the Y-axis in Fig. 12e–h, respectively). Most location errors in those areas are less than 2 m. A larger error can be found, where the ray path density is lower in the traveling time tomography. Compared to the location results using the homogenous velocity model, the location accuracy is much higher and continually improves with more drilling blasting sources added to the P-wave velocity tomography.
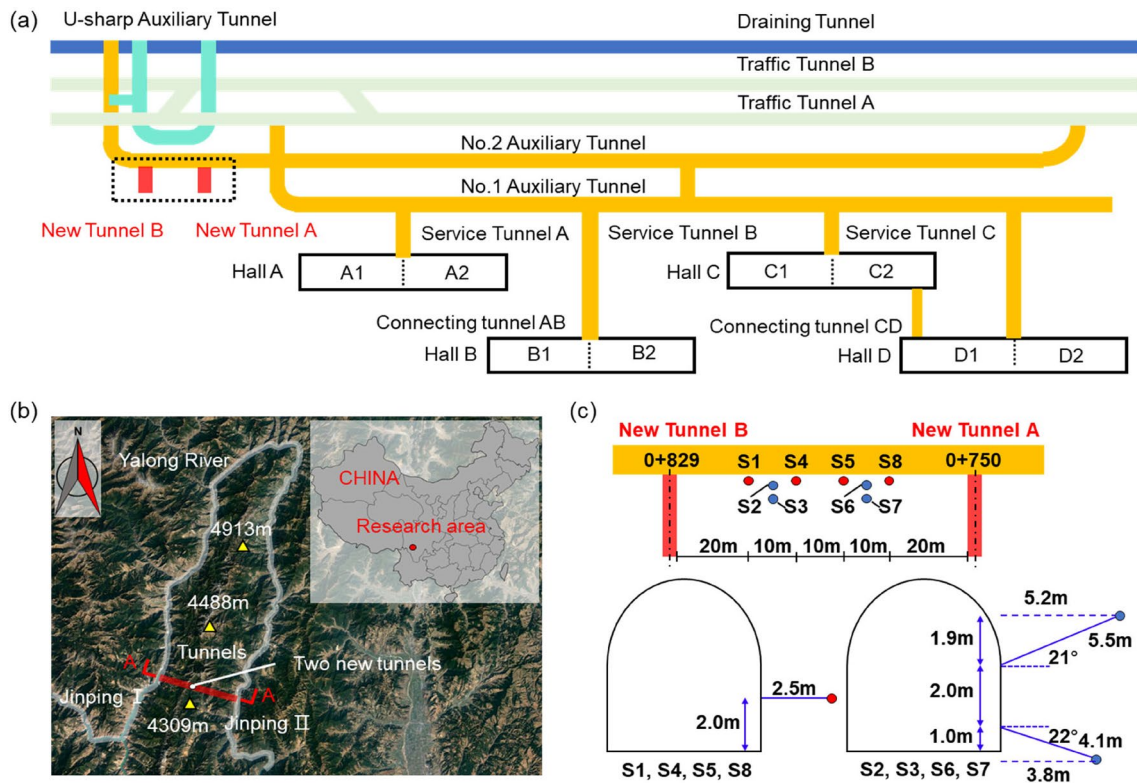
Fig. 13 Project background of deep buried tunnels in Jinping China and the MS monitoring setup of two new tunnels: **a** layout of CJPL-II, **b** location of Jinping China, and **c** MS monitoring setup

4 Case Study

MS monitoring of two new tunnels with a buried depth of 2400 m in China Jinping Underground Laboratory Phase II (CJPL-II) was conducted to warn of rockburst disasters. We inverted the heterogeneous P-wave velocity model of the monitoring area based on drilling and blasting source data analysis. Then, the blasting sources with a known location were used to test the proposed location method.

4.1 Project Background and MS Monitoring Setup

CJPL-II is one of the deepest underground laboratories on the Yalong River in Sichuan Province, China (Li et al. 2021; Zheng et al. 2021). The CJPL-II has a maximum burial depth of 2525 m. The surrounding rock of the tunnel and laboratories mainly consists of marble with high strength and brittleness. The maximum principal stress of the surrounding rock is 69.20 MPa (Jiang et al. 2021). Based on several previous studies, rockbursts frequently occur during the excavation of tunnels and laboratories (Feng et al. 2015b). The layout of the 8 caverns of CJPL-II and their connection to the traffic

tunnels are shown in Fig. 13a. Two new tunnels were proposed at the no. 2 auxiliary tunnel, as shown in the dashed square. The two tunnels were constructed at the same time using the drilling and blasting method. Thus, the monitoring network was installed in the middle of two tunnels, so that the MS events occurring around the drilling face of two tunnels could be monitored using one equipment system. A SinoSeism (SSS) MS source monitoring system (Chen et al. 2021) with a 32-bit A/D acquisition apparatus was deployed in this case. Eight sensor monitoring networks were designed, as shown in Fig. 13c. The nearest sensor was 20 m from the tunnel, where the blasting wave would not damage the sensors. The inversion of the velocity model and location of the MS source were simplified to a 2D issue due to the plane-like monitoring network and objective area.

4.2 Inversion of the Velocity Model

Blasting signals were collected to invert velocity models of the monitoring area. The locations of the 14 blasting sources (7 in tunnel A and 7 in tunnel B) are summarized in

Table 2 Calculation of t_0 of the different drilling blast sources in the field case

Number of tunnel	Coordinate of known blast source (m)		S-wave arrival time of No.1 sensor (year/month/day h:min:s)	S-wave absolute travelling time of No.1 sensor (s)	Time of drilling blast source in tunnel A (year/month/day h:min:s)
Tunnel A	A1	(750, 2)	2021/9/7 18:56:35.60755	0.01607	2021/9/7 18:56:35.59148
	A2	(750, 4.5)	2021/9/15 01:09:13.27175	0.01582	2021/9/15 01:09:13.25593
	A3	(750, 7)	2021/9/20 00:04:14.56410	0.01559	2021/9/20 00:04:14.54851
	A4	(750, 10.5)	2021/9/23 20:52:23.54895	0.01550	2021/9/23 20:52:23.53345
	A5	(750, 14)	2021/9/30 13:23:56.23615	0.01575	2021/9/30 13:23:56.22040
	A6	(750, 17.5)	2021/10/3 21:34:45.70745	0.01616	2021/10/3 18:56:35.69129
	A7	(750, 20)	2021/10/5 14:03:42.57210	0.01644	2021/10/5 18:56:35.55566

Number of tunnel	Coordinate of known blast source (m)		S-wave arrival time of No.8 sensor (year/month/day h:min:s)	S-wave absolute travelling time of No.8 sensor (s)	Time of drilling blast source in tunnel B (year/month/day h:min:s)
Tunnel B	B1	(829, 2)	2021/9/1 23:19:51.64450	0.01592	2021/9/1 23:19:51.62853
	B2	(829, 4.5)	2021/9/6 18:41:53.89455	0.01568	2021/9/6 18:41:53.87887
	B3	(829, 9)	2021/9/12 22:55:12.36590	0.01535	2021/9/12 22:55:12.35055
	B4	(829, 12.5)	2021/9/16 00:20:43.35950	0.01547	2021/9/16 00:20:43.34403
	B5	(829, 15)	2021/9/18 23:50:23.44895	0.01572	2021/9/18 23:50:23.43323
	B6	(829, 18)	2021/9/21 18:10:32.12355	0.01608	2021/9/21 18:10:32.10747
	B7	(829, 20)	2021/9/28 19:30:53.35610	0.01630	2021/9/28 19:30:53.33980
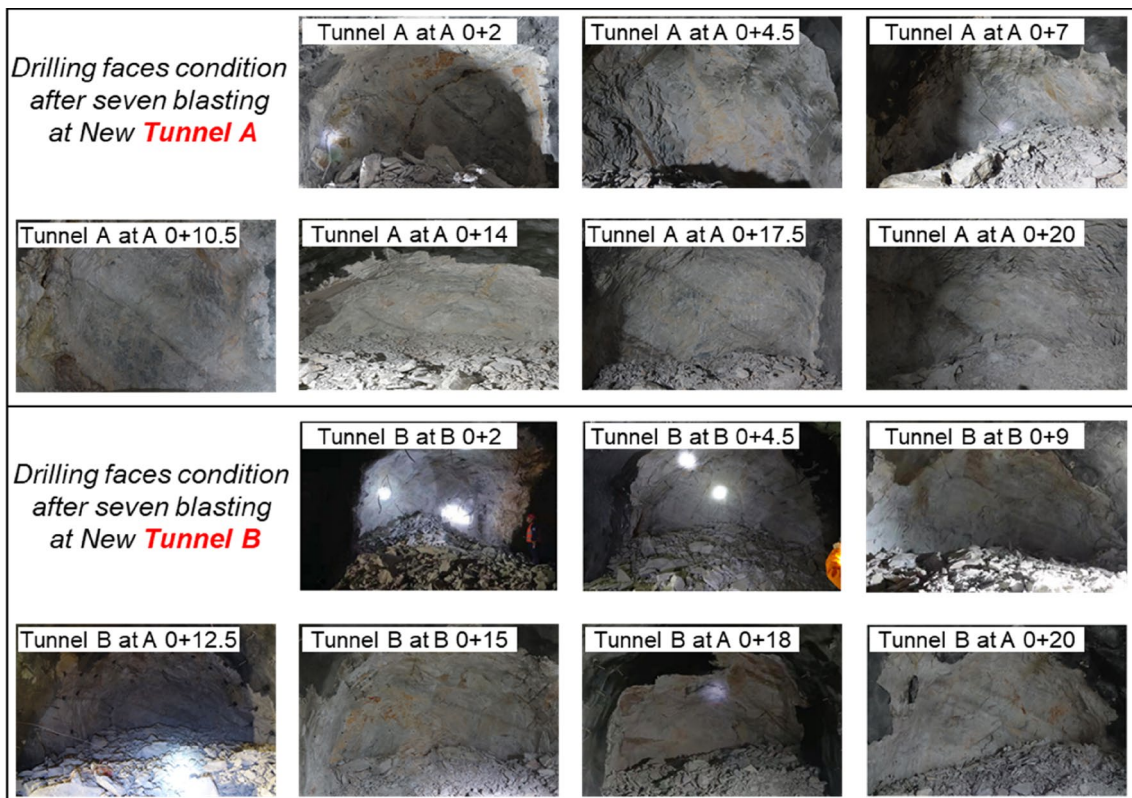
Fig. 14 Drilling face conditions after blasting of two new tunnels
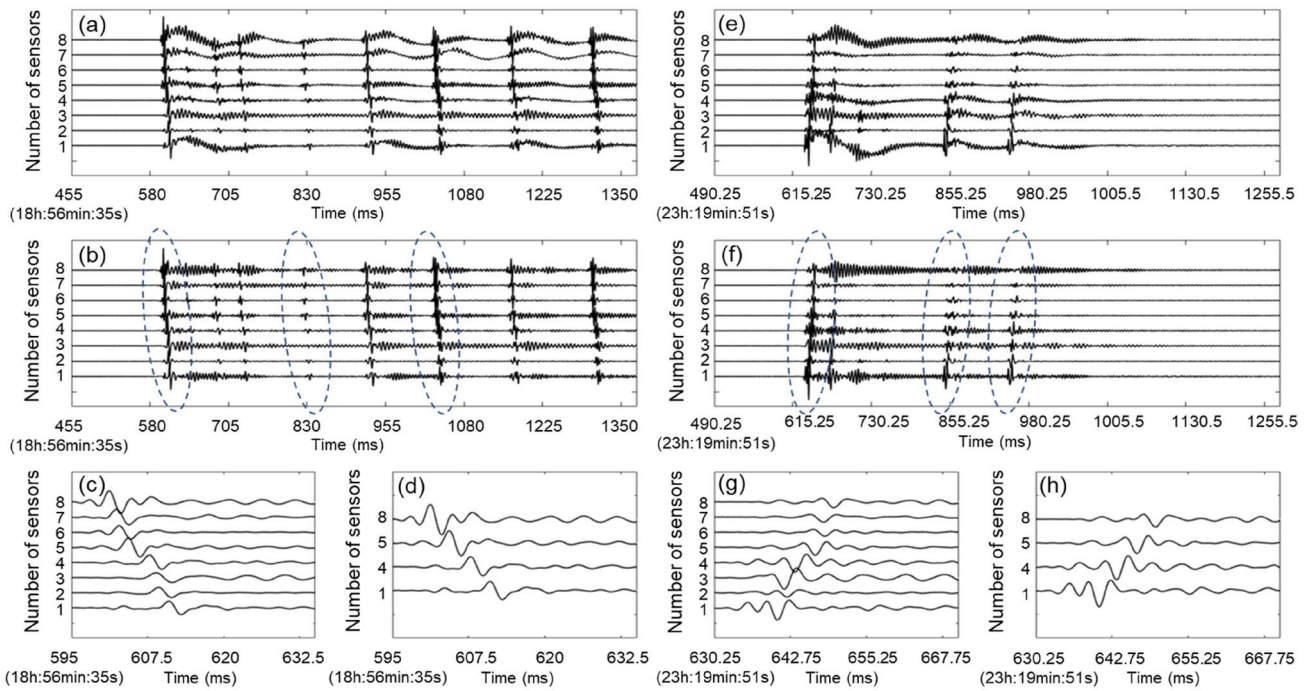
Fig. 15 Blasting signal processing of the first source in tunnels A and B (A1 and B1 in Table 2). **a** Original signal of blasting source A1. **b** Processed signal of blasting source A1. **c** Time slice of the first pulse in **a**. **d** Time slice of channels S1, S4, S5, and S8. **e** Original signal of blasting source B1. **f** Processed signal of blasting source B1 in **a**. **g** Time slice of the first pulse in **e**. **h** Time slice of channels S1, S4, S5, and S8 in **e**

Fig. 16 Dispersion curve calculated by recordings of S1, S4, S5 and S8. **a** Dispersion curve calculated from blasting tunnel data of tunnel A. **b** Dispersion curve calculated from blasting source data of tunnel B
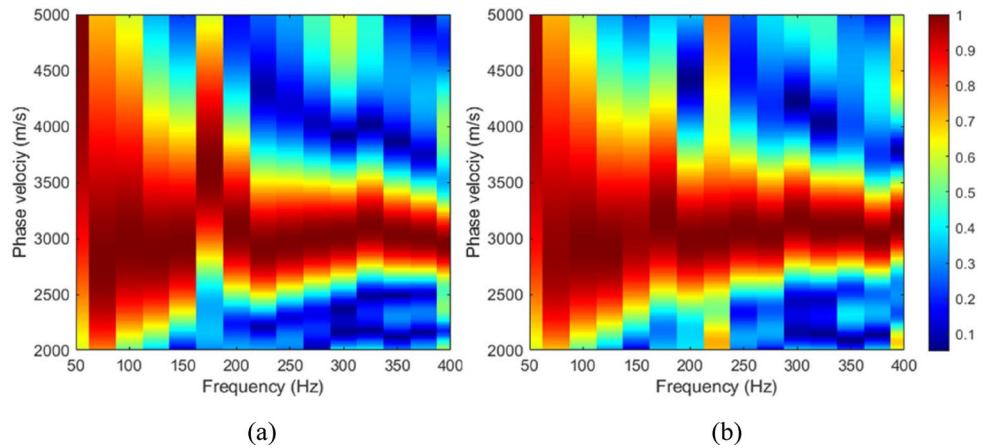
Table 2. The geological conditions of the drilling faces during construction are shown in Fig. 14. Most tunnel drilling faces were grayish-white fine crystal marble. The rock mass was blocky with general integrity. Part of the rock mass was rusty yellow due to ferromanganese filling. The rock fracture was dry, fresh and not weathered. There was no noticeable sound when taking photos. The MS monitoring results suggested a minor rockburst risk at tunnel B 0 + 4.5 and a low rockburst risk at other stages. The drilling face at tunnel B 0 + 4.5 was sprayed, anchored and grouted in the actual project. There was no rock burst during the whole construction process. In this study, four sensors with the same height
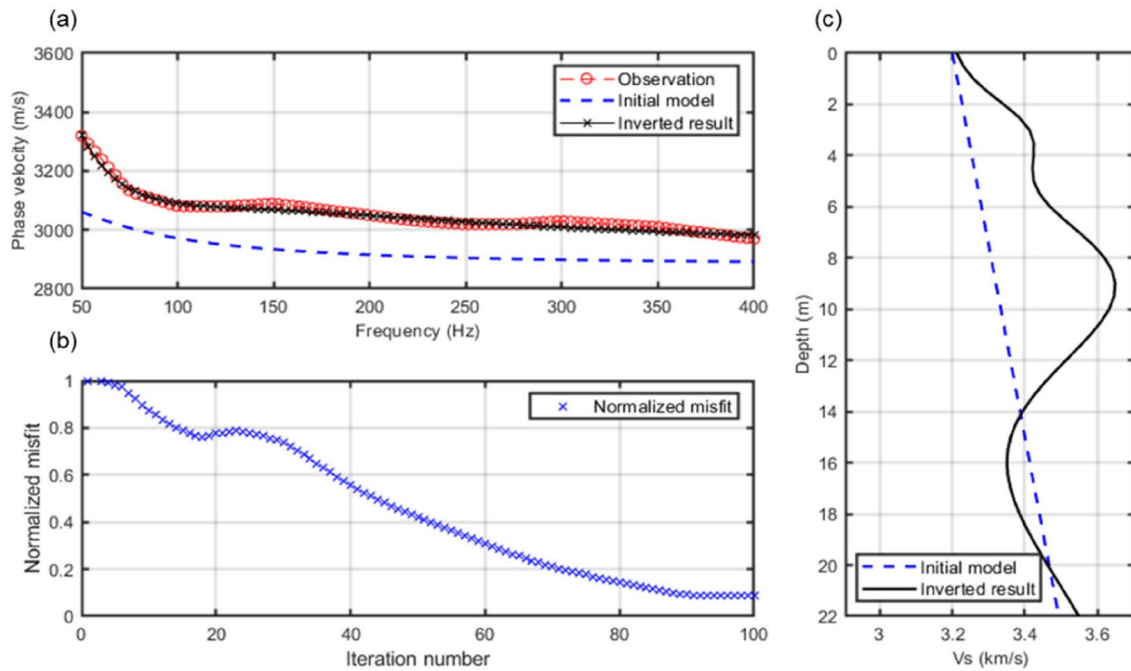
Fig. 17 Inversion process of the dispersion curve of field data: **a** dispersion curve comparison at the 100th iteration, **b** misfit evolution, and **c** S-wave velocity comparison at the 100th iteration
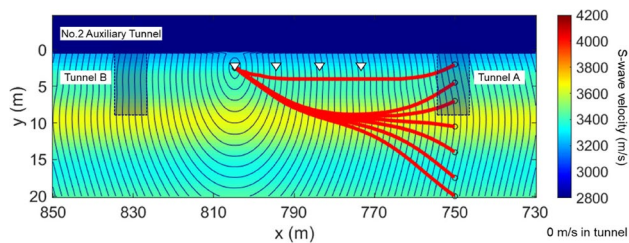
Fig. 18 Determining t_0 of blasting source A1 by backpropagation of the S-wave from S1 sensors

(S1, S4, S5 and S8 in Fig. 13c) were used for surface wave dispersion analysis, and all eight sensors were considered during the P-wave velocity tomography.

4.2.1 Data Processing of the Blasting Signal

The signal processing of the first blasting source signal in tunnels A and B (A1 and B1 in Table 2) is shown in Fig. 15. The original signals in Fig. 15a, e show prominent low-frequency noise in traces S1, S4 and S8, which is caused by the electric interference of the sensors. An FIR bandpass frequency filter is applied to remove the low-frequency noise. Multiple pulses can be observed from the filtered waveform profile in Fig. 15b, f, which indicates that multiple blast sources were transmitted independently and can be analyzed separately. The time slice of the first pulse was extracted, as

shown in Fig. 15c, g, to investigate waveform characteristics. The first arrival of the P-wave in all the traces is clearly identified. The P-wave and S-wave gradually separate as the offset increases. Thus, the first arrival of the S-wave is difficult to determine in several near offset traces. However, in the further offset trace (S1–S4 in the tunnel A data set, S5–S8 in the tunnel B data set), it is easy to identify the first break of the S-wave arrival. Note that the same horizontal position pairs of S2 and S3 and S6 and S7 have highly similar waveform and arrival time information, which verifies that the 2D assumption is applicable in the inversion and location.

4.2.2 Dispersion Analysis

The dispersion curves are extracted from Fig. 15d, h using the tunnel A and B blasting source data. The two dispersion energy distributions in Fig. 16a, b present similar sharpness, because they reflect the same velocity–depth curve. The dispersion phenomenon is shown in Fig. 16, which indicates a velocity change with the depth of the surrounding rock. The two dispersion curves suggest a lower velocity at higher frequency and a high-velocity area at 175 Hz and 50 Hz.

The proposed improved perturbational inversion method applies the average of two dispersion curves to invert the S-wave velocity model. Gaussian smooth and cubic spline interpolation are applied to preprocess the dispersion curve. The initial model for inversion linearly varies from 3200 to 3500 m/s (the blue dashed line in Fig. 17c). The misfits

Table 3 P-wave traveling time of 14 blasting sources in the field case

Number of tunnels	Number of drilling blast	P-wave travelling time of No.1 Sensor (s)	P-wave travelling time of No.2 Sensor (s)	P-wave travelling time of No.3 Sensor (s)	P-wave travelling time of No.4 Sensor (s)	P-wave travelling time of No.5 Sensor (s)	P-wave travelling time of No.6 Sensor (s)	P-wave travelling time of No.7 Sensor (s)	P-wave travelling time of No.8 Sensor (s)
Tunnel A	A1	0.00979	0.00886	0.00883	0.00821	0.00643	0.00551	0.00549	0.00465
	A2	0.00965	0.00872	0.00868	0.00807	0.00632	0.00539	0.00536	0.00457
	A3	0.00957	0.00863	0.00860	0.00799	0.00627	0.00533	0.00529	0.00455
	A4	0.00957	0.00864	0.00860	0.00801	0.00632	0.00538	0.00533	0.00466
	A5	0.00974	0.00881	0.00876	0.00818	0.00651	0.00558	0.00552	0.00489
	A6	0.01003	0.00910	0.00905	0.00849	0.00684	0.00591	0.00584	0.00526
	A7	0.01028	0.00935	0.00930	0.00874	0.00710	0.00618	0.00610	0.00556
Tunnel B	B1	0.00450	0.00532	0.00530	0.00613	0.00789	0.00865	0.00862	0.00961
	B2	0.00441	0.00520	0.00517	0.00601	0.00776	0.00851	0.00848	0.00947
	B3	0.00444	0.00515	0.00510	0.00598	0.00767	0.00841	0.00837	0.00937
	B4	0.00461	0.00528	0.00523	0.00611	0.00779	0.00852	0.00848	0.00948
	B5	0.00481	0.00546	0.00540	0.00629	0.00795	0.00868	0.00864	0.00964
	B6	0.00514	0.00576	0.00569	0.00658	0.00822	0.00895	0.00890	0.00990
	B7	0.00539	0.00599	0.00591	0.00681	0.00844	0.00916	0.00911	0.01011
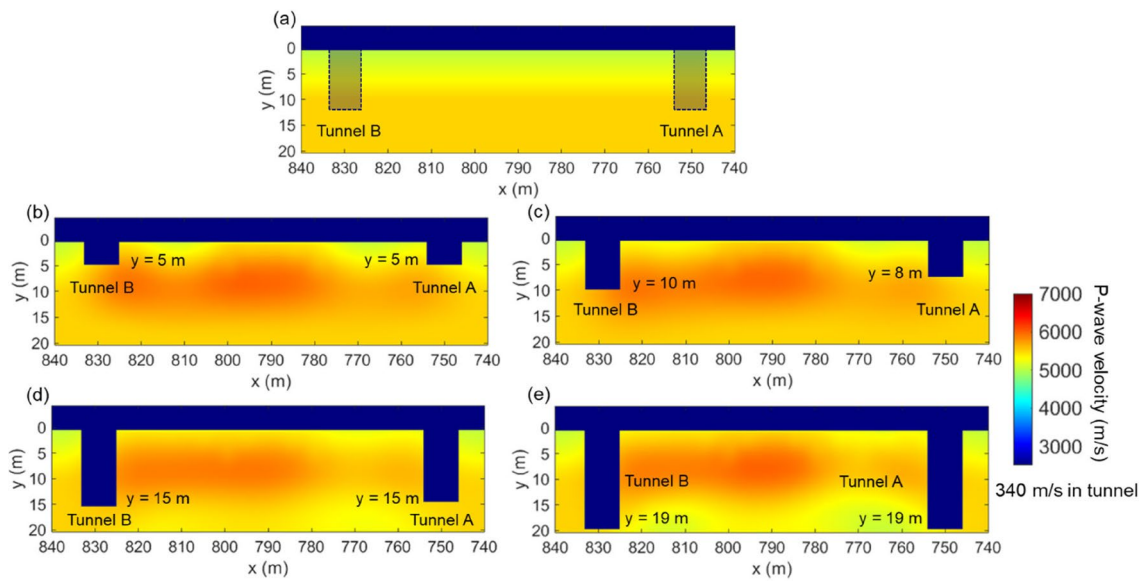
Fig. 19 Results of P-wave traveling time tomography during drilling: **a** initial model. **b** Tomography results from blasting sources A1, A2, B1, and B2. **c** Tomography results from blasting sources A1–A3 and B1–B3. **d** Tomography results from blasting sources A1–A5 and B1–B5. **e** Tomography results from blasting sources A1–A7 and B1–B7

between the observed and simulated dispersion curves decrease rapidly and converge at 0.11 normalized misfits after the 100th iteration (Fig. 17a, b). The inverted S-wave presents a low-velocity zone in the depth range from the surface to 10 m, which is consistent with the preset true S-wave velocity model. The inverted S-wave velocity–depth curve is shown in Fig. 17c. The inverted results suggest a 2.8 m EDZ zone of the surrounding rock. Intact rock of high S-wave velocity can be found at approximately 9 m. Note

that a lower velocity area indicates broken rock or developed discontinuities.

Ray path tracing of wave backpropagation from the S1 sensor to the sources is used to estimate t_0 of the blasting sources in tunnel A. The FMM calculates the traveling time and their isochrones, as shown in Fig. 18. The wave propagation path on the heterogeneous velocity model can be traced by searching the normal direction of the isochrones. The arrival time of the S-wave and traveling time of the S1 and

Fig. 20 Location accuracy test of known blasting sources using different inverted velocity models. **a** Location error of the blasting source in Tunnel A. **b** Location error of the blasting source in Tunnel B

S8 sensors are used to calculate t_0 of the blasting sources in tunnels A and B by Eq. (1), respectively. The results are presented in Table 2.

4.2.3 P-Wave Traveling Time Tomography

The calculated t_0 of the blasting sources was used to obtain the P-wave traveling time. The P-wave traveling time of every sensor and source is summarized in Table 3. The initial model of P-wave traveling time tomography is shown in Fig. 19a, which linearly varies from 5000 to 5500 m/s in the depth range from 0 to 10 m. The inversion is divided into four steps using differen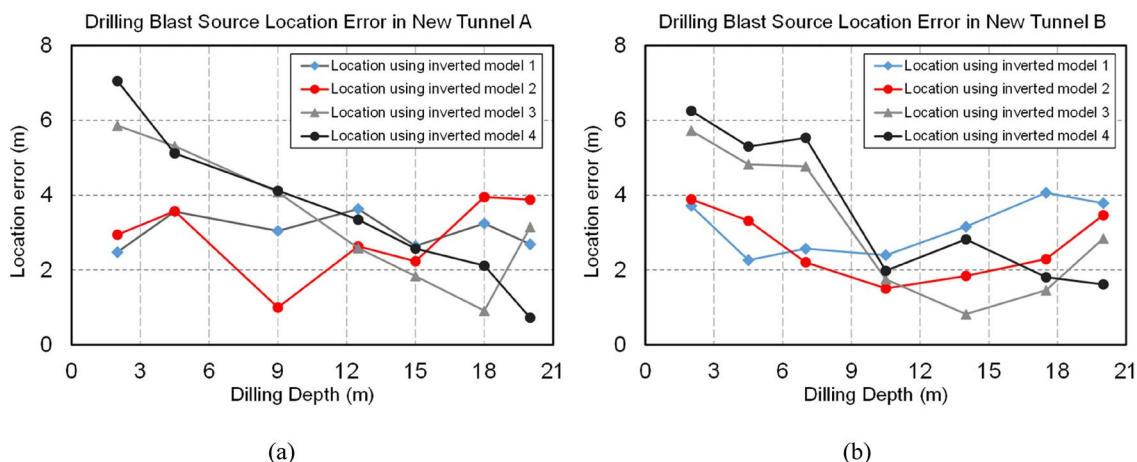t blasting sources. Step one uses blasting sources A1, A2, B1, and B2. Step two uses blasting sources A1–A3 and B1–B3. Step three uses blasting sources A1–A5 and B1–B5. Step four uses blasting sources A1–A7 and B1–B7. The inverted P-wave velocity models of different steps are shown in Fig. 19b–e. All the inverted velocity models can identify the EDZ. A higher velocity area can be observed in the depth range from 5 to 10 m, which suggests an intact rock layer. The inverted velocity models of steps 3 and 4 indicate a lower velocity area at depths from 14 to 20 m. The velocity models in Fig. 19c–e consistently suggest that the velocity of the surrounding rock near tunnel A is lower than that near tunnel B.

4.3 Validation by the Blasting Source Location

No significant rockburst occurred during the tunnel's excavation, although many MS events were monitored. Thus, the 14 blasting source data with known locations are applied to validate the proposed location method. Four velocity models (Fig. 19c–e) obtained at different drilling steps are used to locate the blasting source. The location

results of 14 blasting sources using different velocity models can be found in Appendix Tab le 5. The location errors are concluded in Fig. 20. Most location errors are less than 5 m. The location errors of the deeper drilling sources are lower. The location result using inverted model 1 (Fig. 19c) is shown by the blue line in Fig. 20. The location errors are stable during the whole drilling and less than 4 m. The location using inverted model 2 (Fig. 19d) presents better location accuracy at a depth of 9 m, where the blasting source (9 m and 7 m in depth of tunnels A and B) is newly added to the tomography of model 2. A similar phenomenon can be found in the depth range from 15 to 18 m of inverted model 3 (gray line in Fig. 20) and depth range from 18 to 20 m of inverted model 4 (black line in Fig. 20). When a blasting source is newly added to the tomography process, locating the source and its adjacent space has better accuracy (error less than 2 m).

5 Discussion

Both numerical and field experiments suggest that the location method based on updating the inverted heterogeneous velocity significantly improved the location accuracy. However, the basic assumption, the reason for location error, and the method's potential application need to be pointed out. The aspects of the proposed location method that merit further discussion include the following:

1. Location error analysis
   The factors that affect the location accuracy using the proposed method can be generally divided into two parts: velocity inversion and source location.

During the inversion of the velocity model, the estimation of t_0 is the priority of P-wave traveling tomography. The proposed method uses dispersion analysis to invert an S-wave model and then backtraces the S-wave propagation from the sensors to the source to estimate the t_0 of the blasting source. The basic idea of the proposed method is that both the S-wave and the P-wave have the same trigger time. Moreover, t_0 is not mandatory for dispersion inversion of the surface wave. The estimation error of t_0 is mainly caused by the error of the S-wave velocity inverted by dispersion analysis. The basic assumption of surface wave dispersion inversion is the horizontal layer assumption (Park et al. 1998). Although the S-wave velocity of the EDZ is layered, which is consistent with the assumption of surface wave inversion, the range of the EDZ fluctuates in the axial tunnel direction. If the depth of the EDZ zone changes dramatically, the error in the estimated t_0 increases. A trigger instrument is required to directly record the t_0 blasting source in complex geological conditions, which can completely remove the error in the estimated t_0. The other factor that affects the accuracy of the inverted velocity model is the ray path density of the P-wave in the tomography, which is determined by the limited number of sources and sensors. The gradient mainly updates the velocity model, where the ray path density is high. Due to the acquisition geometry, some areas with no ray path are not updated during the tomography. A smooth Gaussian filter can be applied to mitigate the unbalanced updates for velocity. A study on the weight function of ray path density is meaningful to improve the traveling time tomography algorithm. Meanwhile, significant anisotropy of seismic waves (King and Talebi 2007; Gajek and Malinowski 2021) caused by complicated lithology, structure and stress state also may affect the location error, which is not considered in the proposed velocity inversion and location method.

During the location of the MS source, both the ill-posed monitoring network and 2D simplification affect the location accuracy. The layout of sensors cannot cover the monitoring area due to the limitation of tunnel construction. The MS events occur outside the array of sensors. The double-difference traveling time objective function and the simplex method improve the location convergence speed. However, the linear-like layout of sensors is still sensitive to the MS location source on the same line of the sensor array (e.g., the location results of blasting sources A1 and B1 in Appendix Table 5 and Fig. 20). The location of the MS source is simplified as a 2D problem, because the heterogeneous P- and S-wave velocity models are inverted in 2D using current acquisition geometry. This 2D simplification might induce extra errors. The 3D layout of monitoring sensors can be deployed in the future to invert a 3D heterogeneous velocity model, so that the MS source can be located in a 3D coordinate system.

2. Identifying the first arrival of the P-wave and S-wave

Accurate identification of the first-arrival time of the P-wave and S-wave is critical to traveling time tomography and MS source location. From both numerical and field experimental waveforms in Figs. 6 and 15, it is not difficult to identify the first break of the P-wave. However, the overlap of the P-wave and S-wave challenges clear identification of the arrival of the S-wave for the near-field sensor. Arrival identification based on the instantaneous phase difference between the P- and S-waves can be explored in further studies to mitigate the picking error for both P- and S-wave arrivals.

In this study, only one S-wave arrival time needs to be extracted to estimate the t_0 of the blasting time. Thus, we recommend using the S-wave recorded by the sensor with the farthest offset, where the S-wave and P-wave completely separate, as shown in Figs. 6a, 15c, g. All the P-wave arrival times are suggested to be applied to ensure a sufficient ray path during the P-wave tomography. We use the P-wave arrival of MS sources to calculate their location. Compared to the layered S-wave velocity model, the continuous updating and heterogeneous P-wave velocity model have a higher resolution of the geological structure and can visualize the change in velocity distribution during tunnel excavation.

3. Selection of inverted velocity models

Inverted velocity models of multiple stages can be obtained during tunnel excavation. We test the location accuracy using different inverted velocity models in both numerical and field experimental studies. The detailed location results and their errors are shown in Appendix Tables 4 and 5 and Figs. 12 and 19. Based on the previous knowledge, the location accuracy should be consistently improved using the velocity models inverted by the most blasting sources. However, the location results show that the best resolution is in the depth range, where the blasting source of the corresponding depth is newly added to the tomography. Taking the location using model 4 in the field case (black dot in Fig. 19) as an example, the location of the A7 and B7 blasting sources is the most accurate. One reason is that the monitoring network is more robust for the location of the deeper source. More critically, gradients are mainly updated to the velocity model between newly added sources and sensors during tomography, which mitigates the location error of adjacent areas of these sources. Thus, we suggest selecting the inverted velocity model depending on the monitoring area.

4. Potential application in linear excavated tunnels

The numerical and field experimental study is based on two new tunnels intersected by an exist-

ing tunnel. The EDZ is deeply developed, because the existing tunnel has been constructed for a long time. The EDZ primarily affects the velocity distribution of the surrounding rock in the field case. The proposed method shows its advantages of location accuracy and estimation of EDZ in the intersected tunnel construction. The proposed velocity inversion and location method is also applicable to regular linear excavated tunnels and is an ongoing research topic. The estimation of t_0 of the blasting time is difficult, since the array sensors are much farther from the sources in the linear excavated tunnel scenario. A single inverted S-wave velocity curve is not suitable to be extended to a layered velocity model in the monitoring area. However, a trigger instrument on the blasting source can be deployed to measure t_0 directly. For P-wave traveling time tomography, a moving array of sensors provides an even better acquisition geometry than the case reported in this study. The proposed location algorithm can be easily extended to a 3D version using 3D FMM and simplex code if the velocity model can be inverted using a 3D monitoring network.

6 Conclusion

In this paper, we developed an inverted heterogeneous velocity model for microseismic source location in deep buried tunnels. An improved perturbational dispersion inversion of surface wave and adjoint-state traveling time tomography method using blasting data was provided to obtain a heterogenous P-wave velocity model. A double-difference simplex-based method was introduced for MS source location. A numerical study and a field case were conducted to test the accuracy of the proposed location method. The following conclusions can be drawn:

1. The EDZ significantly changes the wave propagation path in deeply buried tunnels. It is necessary to invert the velocity model of the EDZ before MS location. The drilling and blasting source data can be used for seismic exploration. The dispersion of surface waves traveling along the sidewall of the tunnel makes it possible to invert the S-wave velocity of the EDZ. An improved perturbational dispersion inversion method is developed by combining modified TLM forward simulation and perturbational inversion. The inversion method can estimate the S-wave velocity model and the EDZ depth.

2. P-wave first-arrival tomography of the blasting source can be used to obtain a heterogeneous P-wave veloc-

ity model. The starting time t_0 of blasting sources is estimated using S-wave back propagation tracing by the FMM on the inverted S-wave model. Adjoint-state first-arrival tomography was provided in this paper. The FMM solves the eikonal equation and forward-simulates travel time. The adjoint-state method is introduced to compute the gradient of the misfit function without introducing Fréchet derivatives during inversion. Updating velocity models are inverted when new blasting source data are added to tomography.

3. An objective function of MS source location is provided using the L2 norm of the double difference of the traveling time. The FMM is deployed to forward-simulate the traveling time of the inverted heterogeneous P-wave velocity model and calculate the double-difference traveling time in the objective function. The double-difference function removes the parameter t_0 of the MS source and improves the stability of the location method. The simplex method is introduced as a nonlinear optimization technique to search for the minimum misfit of the objective function and the best-fit location.

4. A numerical study based on a realistic tunnel model was conducted to test the location accuracy of the proposed method. The surface wave dispersion inverts a layered S-wave model and successfully estimates t_0 of the blasting source by the FMM. P-wave first-arrival time tomography imaging is used to provide more detailed heterogeneous velocity models. Sixty-four MS sources around the tunnel drilling face are simulated to test the accuracy of the proposed location method. The results show that location by the inverted heterogenous velocity model significantly improves the location accuracy compared to that of the homogeneous velocity model.

5. A field experiment was conducted at two new tunnels with a buried depth of 2400 m in China Jinping Underground Laboratory Phase II, one of the deepest underground laboratories. We continually inverted the heterogeneous P-wave velocity model of the monitoring area during tunnel drilling based on the analysis of the blasting source data. Blasting sources with a known location were used to test the proposed location method. The results showed that most location errors were less than 5 m using inverted velocity models. The location error can be less than 2 m if the updated inverted velocity model is appropriately selected.

Appendix

See Tables 4 and 5.

Table 4 Location results of the MS source using different velocity model in the numerical study

| True location of MS source | | True velocity model | | Homogeneous velocity model | | | | | | Inverted velocity model | | | | | | | |
X (m)	Y (m)	Y (m)	X (m)	4500 m/s Y (m)	4500 m/s X (m)	5000 m/s Y (m)	5000 m/s X (m)	4500 m/s Y (m)	4500 m/s X (m)	Step 1 (Fig. 10c) Y (m)	Step 1 (Fig. 10c) X (m)	Step 2 (Fig. 10d) Y (m)	Step 2 (Fig. 10d) X (m)	Step 3 (Fig. 10e) Y (m)	Step 3 (Fig. 10e) X (m)	Step 4 (Fig. 10f) Y (m)	Step 4 (Fig. 10f) X (m)
8.000	5.000	5.047	8.076	13.864	1.875	8.914	2.963	1.801	17.061	5.755	8.686	5.058	12.013	3.947	15.687	17.061	19.373
10.000	5.000	5.114	10.113	13.308	3.260	9.237	1.548	1.492	25.043	5.504	11.348	5.081	10.396	3.853	17.935	25.043	19.547
12.000	5.000	4.933	11.450	12.940	5.175	9.467	0.622	1.240	29.318	5.377	13.491	5.144	13.743	3.985	19.678	29.318	19.428
14.000	5.000	4.938	13.568	12.398	6.735	9.371	2.046	1.492	26.654	5.388	14.122	4.985	14.206	3.925	21.043	26.654	20.050
16.000	5.000	5.174	16.132	13.937	2.905	9.103	4.672	1.741	28.165	5.476	15.653	5.348	14.214	3.890	22.346	28.165	23.421
18.000	5.000	5.092	18.176	14.084	2.726	9.250	5.170	2.754	22.836	5.559	17.612	5.345	15.610	4.170	22.230	22.836	24.518
20.000	5.000	5.153	20.092	13.987	3.571	8.361	11.494	2.735	25.498	5.403	20.070	4.909	23.075	4.091	24.260	25.498	23.918
22.000	5.000	5.180	21.672	14.763	4.001	7.851	14.629	2.472	28.485	5.582	20.638	5.149	23.246	4.321	24.010	28.485	25.255
8.000	7.000	7.159	8.011	17.236	0.142	12.851	0.071	6.874	9.255	7.713	9.665	7.053	9.842	5.548	15.631	9.255	10.398
10.000	7.000	7.213	10.876	17.489	0.885	10.904	8.392	6.498	12.129	7.486	12.197	7.101	11.666	5.671	14.797	12.129	14.404
12.000	7.000	7.129	12.003	17.607	0.793	13.187	3.821	6.609	13.304	7.102	16.613	6.945	14.201	5.744	16.740	13.304	19.907
14.000	7.000	6.961	13.138	17.604	1.784	13.609	0.833	6.231	17.160	7.259	16.872	6.718	17.928	5.670	18.243	17.160	19.917
16.000	7.000	6.840	15.054	16.584	5.890	12.697	5.879	6.133	19.172	7.609	15.648	6.829	18.368	5.904	18.268	19.172	19.995
18.000	7.000	7.060	18.398	17.698	4.139	12.189	9.092	5.270	23.874	7.186	21.334	7.071	18.977	6.025	20.207	23.874	19.930
20.000	7.000	7.127	20.180	17.619	5.892	10.968	14.689	5.879	22.869	7.221	21.825	6.949	22.794	6.169	21.826	22.869	21.768
22.000	7.000	7.199	22.036	16.067	11.398	10.174	18.933	6.111	24.219	7.248	23.484	6.987	23.941	6.081	24.472	24.219	24.107
8.000	9.000	9.068	6.692	19.524	3.058	15.712	2.893	10.753	7.058	9.595	12.030	8.670	13.392	7.770	12.095	7.058	14.146
10.000	9.000	9.070	10.048	18.723	6.301	15.481	4.557	10.195	10.536	9.475	13.496	9.354	11.236	7.537	14.597	10.536	13.438
12.000	9.000	9.016	12.182	19.925	4.497	15.434	5.492	10.079	12.249	9.023	16.674	9.139	14.131	7.749	15.980	12.249	14.305
14.000	9.000	9.007	14.023	19.793	5.678	14.999	8.339	9.231	16.183	9.735	17.241	9.183	15.663	7.335	20.428	16.183	14.483
16.000	9.000	9.009	16.072	20.000	6.811	14.347	11.526	8.906	19.354	9.346	18.313	9.322	16.621	8.254	16.834	19.354	16.282
18.000	9.000	9.004	18.120	19.934	8.321	13.567	15.190	8.972	20.692	10.000	18.372	9.564	17.952	8.339	18.693	20.692	18.110
20.000	9.000	9.050	20.105	18.365	13.169	13.400	16.916	9.173	21.738	10.324	18.260	9.146	21.043	7.900	22.796	21.738	21.734
22.000	9.000	9.108	22.027	17.128	16.741	12.444	20.979	8.873	23.924	9.464	22.549	9.074	23.377	8.239	23.277	23.924	22.545
8.000	11.000	11.125	8.086	18.303	12.331	18.497	3.675	12.914	9.847	11.343	13.889	11.617	8.981	9.649	11.719	9.847	9.201
10.000	11.000	11.149	10.095	19.729	10.607	17.871	6.913	10.324	14.161	11.281	15.273	11.922	10.315	10.425	8.611	14.161	11.566
12.000	11.000	11.215	12.061	19.232	12.477	17.309	9.090	11.517	16.537	11.862	19.949	11.456	13.643	10.379	12.569	16.537	12.834
14.000	11.000	11.128	14.085	20.000	12.265	17.827	9.900	11.800	16.950	11.303	18.008	11.208	14.650	10.235	14.738	16.950	15.524
16.000	11.000	11.372	15.985	19.900	13.936	15.775	15.629	11.540	19.650	11.121	20.368	11.558	17.087	10.693	15.968	19.650	16.716
18.000	11.000	11.131	18.273	19.655	15.666	16.080	14.641	11.438	21.026	12.145	22.658	11.781	18.540	9.900	20.602	21.026	18.315
20.000	11.000	11.041	20.023	19.409	17.404	15.389	19.830	11.174	23.383	11.073	23.361	11.346	21.554	10.006	22.307	23.383	20.339
22.000	11.000	11.133	22.160	18.961	19.641	14.628	22.491	11.210	24.908	10.990	25.287	11.466	22.909	10.020	23.946	24.908	21.718
8.000	13.000	13.073	8.020	19.708	14.248	19.128	8.767	14.936	11.288	14.224	10.820	13.922	9.526	12.383	7.682	11.288	6.724
10.000	13.000	13.072	9.867	19.934	14.754	19.211	9.891	13.944	15.026	13.757	14.317	13.669	12.347	12.463	10.421	15.026	7.903

Table 4 (continued)

| True location of MS source | | True velocity velocity model | | Homogeneous velocity model | | | | | | Inverted velocity model | | | | | | | |
| | | | | 4500 m/s | | 5000 m/s | | 4500 m/s | | Step 1 (Fig. 10c) | | Step 2 (Fig. 10d) | | Step 3 (Fig. 10e) | | Step 4 (Fig. 10f) | |
Y (m)	X (m)	Y (m)	X (m)	Y (m)	X (m)	Y (m)	X (m)	Y (m)	X (m)	Y (m)	X (m)	Y (m)	X (m)	Y (m)	X (m)	Y (m)	X (m)
13.000	12.000	12.963	13.096	19.914	16.358	17.686	14.210	13.174	18.201	13.087	17.211	13.891	13.315	12.584	12.151	18.201	11.963
13.000	14.000	13.249	13.288	19.924	17.138	17.666	15.746	12.989	20.008	12.933	19.393	13.609	15.988	12.613	14.451	20.008	12.348
13.000	16.000	13.034	16.025	20.000	18.160	17.071	18.492	13.079	21.027	13.407	21.123	13.293	18.662	13.317	14.451	21.027	15.300
13.000	18.000	13.267	17.915	20.000	19.678	17.037	19.817	13.026	22.678	12.255	23.015	13.981	20.770	12.478	17.388	22.678	17.621
13.000	20.000	13.043	20.090	19.965	21.312	16.463	22.286	12.444	25.319	12.604	24.079	13.490	21.879	12.439	21.429	25.319	18.164
13.000	22.000	13.169	22.145	20.000	22.578	16.444	23.687	12.463	26.980	11.919	27.036	14.190	22.172	13.507	20.860	26.980	22.169
15.000	8.000	14.947	8.883	19.101	18.037	19.916	12.197	15.797	14.778	15.833	14.029	17.686	5.961	15.013	6.963	14.778	3.227
15.000	10.000	15.221	9.293	19.997	18.922	19.876	13.509	14.915	17.734	15.154	16.074	15.953	12.285	15.273	8.883	17.734	6.929
15.000	12.000	15.147	12.042	19.671	20.222	19.781	15.271	14.981	19.076	14.381	19.159	15.392	15.759	15.460	10.839	19.076	10.122
15.000	14.000	15.195	14.138	19.920	20.882	18.733	18.083	14.344	21.557	14.396	20.693	16.115	15.627	15.848	12.033	21.557	12.454
15.000	16.000	15.222	15.570	19.923	22.139	18.111	20.979	14.474	22.605	14.243	22.269	15.041	19.988	14.687	17.288	22.605	12.690
15.000	18.000	15.160	17.896	19.667	23.601	17.942	22.476	14.661	23.899	15.280	21.960	14.075	21.144	15.531	17.851	23.899	13.875
15.000	20.000	15.059	19.987	19.918	24.686	17.228	24.638	13.903	26.936	14.268	25.483	15.163	23.047	15.139	20.491	26.936	16.758
15.000	22.000	15.022	22.253	19.847	26.441	17.740	25.507	14.196	27.825	14.074	27.178	15.067	24.830	15.841	21.404	27.825	21.427
17.000	8.000	17.085	8.263	19.885	20.896	20.000	16.394	16.095	18.153	16.540	16.211	16.873	13.680	18.879	3.877	18.153	6.444
17.000	10.000	17.002	10.006	20.000	21.668	19.880	17.725	16.357	19.161	16.749	17.105	17.461	14.495	18.650	7.090	19.161	8.990
17.000	12.000	17.025	11.933	19.672	23.424	20.000	18.891	17.096	19.432	16.640	18.850	16.721	17.073	19.059	8.941	19.432	11.898
17.000	14.000	17.065	14.247	19.437	24.747	19.927	20.393	15.899	22.696	16.015	21.333	17.654	17.415	17.666	14.293	22.696	14.562
17.000	16.000	16.979	16.119	19.434	25.810	19.152	22.777	16.404	23.472	16.697	21.794	16.455	21.040	17.649	16.802	23.472	14.586
17.000	18.000	17.079	18.120	19.846	26.432	20.000	23.143	16.699	24.157	16.074	24.186	16.926	22.123	17.350	19.011	24.157	14.906
17.000	20.000	17.080	20.132	19.991	28.330	18.131	26.968	15.395	27.772	16.113	25.770	17.987	22.195	17.925	20.059	27.772	16.584
17.000	22.000	17.041	22.158	19.675	29.209	18.945	27.237	15.795	28.858	16.049	27.310	17.535	24.923	17.364	23.263	28.858	19.284
19.000	8.000	19.374	7.917	19.378	24.097	20.000	19.785	18.518	17.613	17.655	17.724	19.551	13.258	19.826	8.804	17.613	4.144
19.000	10.000	19.222	10.124	18.449	26.408	19.684	21.236	17.907	20.498	18.608	17.170	19.386	15.178	19.671	11.300	20.498	7.798
19.000	12.000	19.013	12.059	19.915	25.775	20.000	22.232	17.735	21.837	17.835	20.099	18.868	17.559	19.617	13.499	21.837	10.170
19.000	14.000	19.115	14.242	20.000	26.159	20.000	23.044	17.323	23.909	17.830	21.952	19.396	18.888	19.929	15.316	23.909	16.810
19.000	16.000	19.251	16.059	19.526	28.289	20.000	24.920	17.181	25.250	17.934	23.364	19.127	20.648	19.964	17.390	25.250	17.450
19.000	18.000	19.116	18.055	20.000	28.716	19.254	26.753	17.160	26.808	17.534	25.098	18.954	22.883	19.158	20.133	26.808	19.199
19.000	20.000	19.026	20.148	19.958	30.417	19.704	27.515	16.627	28.916	17.570	26.595	18.736	24.571	19.824	21.351	28.916	20.447
19.000	22.000	19.179	22.040	19.953	31.323	19.089	29.623	16.881	29.807	17.103	28.695	18.765	26.460	19.979	23.252	29.807	22.562

Table 5 Location of the blasting source in the field case

Number of tunnels	True location of blasting source		Location results using different inverted velocity model							
			Step 1 (Fig. 19b)		Step 2 (Fig. 19c)		Step 3 (Fig. 19d)		Step 4 (Fig. 19e)	
	Y (m)	X (m)	Y (m)	X (m)	Y (m)	X (m)	Y (m)	X (m)	Y (m)	X (m)
Tunnel A	2.000	829.000	2.463	832.689	2.932	832.781	3.258	834.585	0.356	822.964
	4.500	829.000	4.755	826.750	4.536	825.682	5.258	824.236	4.575	823.699
	7.000	829.000	7.143	831.569	7.759	826.925	8.470	824.459	8.090	823.572
	10.500	829.000	10.116	831.366	10.527	830.507	10.794	830.728	11.412	827.242
	14.000	829.000	12.625	831.845	15.738	828.392	14.090	829.815	16.457	830.388
	17.500	829.000	15.235	832.376	18.254	826.833	16.912	830.337	18.890	827.843
	20.000	829.000	17.757	832.053	18.103	831.903	18.430	831.371	19.319	830.466
Tunnel B	2.000	750.000	1.398	747.595	2.627	747.122	2.106	755.860	1.449	757.035
	4.500	750.000	4.501	753.562	4.683	753.569	5.058	755.284	4.541	755.121
	9.000	750.000	8.887	746.954	9.727	750.686	8.937	745.920	9.609	754.077
	12.500	750.000	11.439	746.525	13.322	752.501	11.742	747.529	12.960	753.316
	15.000	750.000	14.363	752.565	14.985	752.235	15.986	751.549	15.355	752.549
	18.000	750.000	18.241	753.237	17.685	753.941	17.432	749.286	18.999	751.867
	20.000	750.000	18.853	747.565	18.822	746.304	18.251	747.382	19.471	749.505

Declarations

Conflict of Interest The authors declare that they have no known competing financial interests or personal relationships that could have appeared to influence the work reported in this paper.

References

Bohlen T (2002) Parallel 3-D viscoelastic finite difference seismic modelling. Comput Geosci 28(8):887–899

Castellanos F, Van der Baan M (2015) Dynamic triggering of microseismicity in a mine setting. Geophys J Int 202(2):728–737

Chen BR, Li T, Zhu XH et al (2021) Microseismic source location method based on a velocity model database and statistical analysis. Arab J Geosci 14(19):1–16

Collins DS, Toya Y, Pinnock I et al (2014) 3D velocity model with complex geology and voids for microseismic location and mechanism. In: Deep mining 2014: Proceedings of the seventh international conference on deep and high stress mining. Australian Centre for Geomechanics, 2014, pp 681–688

Czarny R, Malinowski M, Chamarczuk M et al (2021) Dispersive seismic waves in a coal seam around the roadway in the presence of excavation damaged zone. Int J Rock Mech Min Sci 148:104937

Dai F, Li B, Xu N et al (2017) Microseismic monitoring of the left bank slope at the Baihetan hydropower station. China Rock Mech Rock Eng 50(1):225–232

Dai F, Jiang P, Xu N et al (2018) Focal mechanism determination for microseismic events and its application to the left bank slope of the Baihetan hydropower station in China. Environ Earth Sci 77(7):1–15

Dong L, Zou W, Li X et al (2019) Collaborative localization method using analytical and iterative solutions for microseismic/acoustic emission sources in the rockmass structure for underground mining. Eng Fract Mech 210:95–112

Dong L, Hu Q, Tong X et al (2020) Velocity-free MS/AE source location method for three-dimensional hole-containing structures. Engineering 6(7):827–834

Dong L, Pei Z, Xie X et al (2022) Early identification of abnormal regions in rock-mass using traveltime tomography. Engineering

Feng GL, Feng XT, Chen BR et al (2015a) Sectional velocity model for microseismic source location in tunnels. Tunn Undergr Space Technol 45:73–83

Feng GL, Feng XT, Chen BR et al (2015b) A microseismic method for dynamic warning of rockburst development processes in tunnels. Rock Mech Rock Eng 48(5):2061–2076

Feng GL, Feng XT, Xiao YX et al (2019) Characteristic microseismicity during the development process of intermittent rockburst in a deep railway tunnel. Int J Rock Mech Min Sci 124:104135

Gajek W, Malinowski M (2021) Errors in microseismic events locations introduced by neglecting anisotropy during velocity model calibration in downhole monitoring. J Appl Geophys 184:104222

Geiger L (1912) Probability method for the determination of earthquake epicenters from the arrival time only. Bull St Louis Univ 8(1):56–71

Gregor J, Benson T (2008) Computational analysis and improvement of SIRT. IEEE Trans Med Imaging 27(7):918–924

Haney MM, Tsai VC (2017) Perturbational and nonperturbational inversion of Rayleigh-wave velocitiesInversion of Rayleigh-wave velocities. Geophysics 82(3):F15–F28

He YF, Chen WT, Chen XF (2006) Normal modes computation by generalized reflection-transmission coefficients method in planar layered half space. Chin J Geophys 49(4):965–973

Hu Q, Dong L (2019) Acoustic emission source location and experimental verification for two-dimensional irregular complex structure. IEEE Sens J 20(5):2679–2691

Jiang R, Dai F, Liu Y et al (2021) Fast marching method for microseismic source location in cavern-containing rockmass:

performance analysis and engineering application. Engineering 7(7):1023–1034

Kausel E, Roësset JM (1981) Stiffness matrices for layered soils. Bull Seismol Soc Am 71(6):1743–1761

King A, Talebi S (2007) Anisotropy effects on microseismic event location. Pure Appl Geophys 164(11):2141–2156

Kroon D-J (2021) Accurate fast marching, MATLAB central file exchange. Retrieved 28 Sept 2021

Leighton F, Blake W (1970) Rock noise source location techniques. US Department of Interior, Bureau of Mines, 1970

Leparoux D, Côte P, Gélis C (2012) EDZ characterization with surface wave analysis: an experimental and numerical study for defining feasibility in the context of the Tournemire platform (France). Near Surf Geophys 10(5):401–411

Li M, Li S, Xiao Y (2011) Rockburst monitoring and dynamic prevention of enlarging excavation in deep underground laboratory. J Eng Geol 30(3):751–759

Li S, Feng XT, Li Z et al (2012) In situ monitoring of rockburst nucleation and evolution in the deeply buried tunnels of Jinping II hydropower station. Eng Geol 137:85–96

Li S, Feng XT, Wang CY et al (2013) ISRM suggested method for rock fractures observations using a borehole digital optical televiewer. Rock Mech Rock Eng 46(3):635–644

Li N, Wang E, Ge M et al (2014) A nonlinear microseismic source location method based on Simplex method and its residual analysis. Arab J Geosci 7(11):4477–4486

Li N, Wang EY, Ge MC (2017) Microseismic monitoring technique and its applications at coal mines: present status and future prospects. J China Coal Soc 42(S1):83–96

Li S, Zheng M, Qiu S et al (2021) Characteristics of excavation disasters and long-term in-situ mechanical behavior of the tunnels in the China Jinping underground laboratory. J Tsinghua Univ (sci Technol) 61(8):842–852

Liu L, Wang Y (2021) Perturbational inversion of fundamental mode Rayleigh wave dispersion curve. In: SEG/AAPG/SEPM first international meeting for applied geoscience & energy. OnePetro, 2021

Ma C, Jiang Y, Li T (2019) Gravitational search algorithm for microseismic source location in tunneling: performance analysis and engineering case study. Rock Mech Rock Eng 52(10):3999–4016

Ma K, Sun X, Zhang Z et al (2022) Intelligent location of microseismic events based on a fully convolutional neural network (FCNN). Rock Mech Rock Eng 1–17

Moler CB, Stewart GW (1973) An algorithm for generalized matrix eigenvalue problems. SIAM J Numer Anal 10(2):241–256

Nelder JA, Mead R (1965) A simplex method for function minimization. Comput J 7(4):308–313

Park CB, Miller RD, Xia J (1998) Imaging dispersion curves of surface waves on multi-channel record. SEG technical program expanded abstracts 1998. Society of Exploration Geophysicists, 1998, pp 1377–1380

Pei D, Quirein JA, Cornish BE et al (2009) Velocity calibration for microseismic monitoring: a very fast simulated annealing (VFSA) approach for joint-objective optimization. Geophysics 74(6):WCB47–WCB55

Prugger AF, Gendzwill DJ (1988) Microearthquake location: a nonlinear approach that makes use of a simplex stepping procedure. Bull Seismol Soc Am 78(2):799–815

Pu Y, Chen J, Jiang D et al (2022) Improved method for acoustic emission source location in rocks without prior information. Rock Mech Rock Eng 1–15

Sei A, Symes WW (1994) Gradient calculation of the traveltime cost function without ray tracing. SEG technical program expanded abstracts 1994. Society of Exploration Geophysicists, 1994, pp 1351–1354

Taillandier C, Noble M, Chauris H et al (2009) First-arrival traveltime tomography based on the adjoint-state method. Geophysics 74(6):WCB1–WCB10

Thurber CH (1985) Nonlinear earthquake location: theory and examples. Bull Seismol Soc Am 75(3):779–790

Waldhauser F, Ellsworth WL (2000) A double-difference earthquake location algorithm: method and application to the northern Hayward fault, California. Bull Seismol Soc Am 90(6):1353–1368

Xiao YX, Feng XT, Hudson JA et al (2016) ISRM suggested method for in situ microseismic monitoring of the fracturing process in rock masses. Rock Mech Rock Eng 49(1):343–369

Xu Y, Xia J, Miller RD (2007) Numerical investigation of implementation of air-earth boundary by acoustic-elastic boundary approach. Geophysics 72(5):SM147–SM153

Yao ZS, Roberts RG, Tryggvason A (1999) Calculating resolution and covariance matrices for seismic tomography with the LSQR method. Geophys J Int 138(3):886–894

Zhao H (2005) A fast sweeping method for eikonal equations. Math Comput 74(250):603–627

Zheng M, Li S, Zhao H et al (2021) Probabilistic analysis of tunnel displacements based on correlative recognition of rock mass parameters. Geosci Front 12(4):101136